

Experimental investigation of the hydrodynamic performance of the ISWEC 1:20 scaled device

*Original*

Experimental investigation of the hydrodynamic performance of the ISWEC 1:20 scaled device / Sirigu, SERGEJ ANTONELLO; Bonfanti, Mauro; Passione, Biagio; Begovic, Ermina; Bertorello, Carlo; Dafnakis, Panagiotis; Bracco, Giovanni; Giorcelli, Ermanno; Mattiazzo, Giuliana. - ELETTRONICO. - (2018), pp. 551-560. ( NAV 2018 Trieste 20 Giugno 2018) [10.3233/978-1-61499-870-9-551].

*Availability:*

This version is available at: 11583/2710055 since: 2018-06-25T14:45:52Z

*Publisher:*

IOS Press

*Published*

DOI:10.3233/978-1-61499-870-9-551

*Terms of use:*

This article is made available under terms and conditions as specified in the corresponding bibliographic description in the repository

*Publisher copyright*

(Article begins on next page)

## Multi-time delay, multi-point linear stochastic estimation of a cavity shear layer velocity from wall-pressure measurements

Daive Lasagna, Matteo Orazi, and Gaetano Iuso

Citation: *Phys. Fluids* **25**, 017101 (2013); doi: 10.1063/1.4774337

View online: <http://dx.doi.org/10.1063/1.4774337>

View Table of Contents: <http://pof.aip.org/resource/1/PHFLE6/v25/i1>

Published by the [American Institute of Physics](#).

---

### Related Articles

Characterization of Hall effect thruster propellant distributors with flame visualization  
*Rev. Sci. Instrum.* **84**, 013302 (2013)

Experimental study on side force alleviation of conical forebody with a fluttering flag  
*Phys. Fluids* **24**, 124105 (2012)

Cantilever anemometer based on a superconducting micro-resonator: Application to superfluid turbulence  
*Rev. Sci. Instrum.* **83**, 125002 (2012)

InAsP-based quantum wells as infrared pressure gauges for use in a diamond anvil cell  
*J. Appl. Phys.* **112**, 074504 (2012)

Note: A versatile, stable, high-resolution readout system for RTD and thermistor sensors  
*Rev. Sci. Instrum.* **83**, 096101 (2012)

---

### Additional information on Phys. Fluids

Journal Homepage: <http://pof.aip.org/>

Journal Information: [http://pof.aip.org/about/about\\_the\\_journal](http://pof.aip.org/about/about_the_journal)

Top downloads: [http://pof.aip.org/features/most\\_downloaded](http://pof.aip.org/features/most_downloaded)

Information for Authors: <http://pof.aip.org/authors>

### ADVERTISEMENT



**Running in Circles Looking  
for the Best Science Job?**

Search hundreds of exciting  
new jobs each month!

<http://careers.physicstoday.org/jobs>

physicstodayJOBS



## Multi-time delay, multi-point linear stochastic estimation of a cavity shear layer velocity from wall-pressure measurements

Davide Lasagna, Matteo Orazi, and Gaetano Iuso<sup>a)</sup>

*Dipartimento di Ingegneria Meccanica e Aerospaziale, Politecnico di Torino, Corso Duca degli Abruzzi 24 Torino, 10129 Italy*

(Received 19 March 2012; accepted 26 November 2012; published online 14 January 2013)

In this paper, the recently introduced multi-time-delay linear stochastic estimation technique is thoroughly described, focusing on its fundamental properties and potentialities. In the multi-time-delay approach, the estimate of the temporal evolution of the velocity at a given location in the flow field is obtained from multiple past samples of the unconditional sources. The technique is applied to estimate the velocity in a cavity shear layer flow, based on wall-pressure measurements from multiple sensors. The cavity flow was investigated by performing simultaneous measurements of a single hot-wire probe, traversed on a fine grid in the shear layer, and of multiple wall-mounted condenser microphones in the cavity region. The paper compares classical high-order single-time-delay estimation approaches with the multi-time-delay technique, which is significantly more accurate as it produces a much lower mean-square estimation error, thus providing a faithful reconstruction of the time-evolution of the velocity field. This improved accuracy is strongly dependent on the number  $n$  of past wall-pressure samples used in the estimate. In this paper, we also demonstrate that the estimated velocity field only contains the signature of the relevant flow mechanisms which correlate well with the wall-pressure, while incoherent components are filtered out. The multi-time-delay approach successfully captures the spatio-temporal dynamics of the velocity fluctuation distribution in the shear layer, as it clearly resolves the dynamics of the relevant flow structures. The effect of the number of sensors used in the estimate was also considered. In general, it was evident that use of more sensors leads to better accuracy, but as the number  $n$  of past values increases, the gain becomes marginal. © 2013 American Institute of Physics. [<http://dx.doi.org/10.1063/1.4774337>]

### I. INTRODUCTION

The stochastic estimation technique is an established tool which offers a quantitative insight into the spatio-temporal evolution of coherent structures and flow patterns.<sup>18</sup> The stochastic estimation framework was first introduced in fluid dynamics by Adrian<sup>1</sup> as a means for approximating the conditional average of the velocity vector  $\mathbf{u}$  given an event  $\mathbf{E}$ , and in order to identify and study coherent structures in homogeneous isotropic turbulent flows. The conditional average was obtained from unconditional statistics by estimating it as a Taylor series of increasing powers of the event. When the expansion is truncated at the linear term the technique is called linear stochastic estimation (LSE).

Since Adrian's work the stochastic estimation technique has been constantly refined and applied to a large amount of flows. Adrian and Moin<sup>2</sup> used an extended event including the local deformation tensor to fully capture the kinematic state of conditional eddies in homogeneous shear flows.

---

<sup>a)</sup>[gaetano.iuso@polito.it](mailto:gaetano.iuso@polito.it).

Guezennec<sup>18</sup> applied the technique to educe coherent structures in turbulent boundary layers. The flow in a jet mixing layer flow was investigated by Cole *et al.*<sup>12</sup> High-order Taylor expansions were considered by Tung and Adrian<sup>36</sup> for conditional eddies in isotropic turbulence, in which the high-order terms appeared to have little influence. By contrast, Murray and Ukeiley,<sup>25</sup> included the quadratic term for the estimation of a supersonic cavity flow and showed a remarkable increase in the fraction of recovered energy through the use of the quadratic stochastic estimation (QSE). Multi-point stochastic estimation, whereby the event vector  $\mathbf{E}$  specifies multiple conditions in more than one location, was also considered, by Cole *et al.*,<sup>12</sup> Guezennec,<sup>18</sup> Hudy *et al.*,<sup>21</sup> Murray and Ukeiley,<sup>26</sup> and others. These authors found that multi-point stochastic estimation leads to a more “realistic” estimate than single-point conditional averages, since the interaction between the events can be observed, unlike single-point estimates where events are taken in isolation.<sup>12</sup>

The stochastic estimation technique has also been used with wall-pressure as the unconditional event. Naguib *et al.*<sup>27</sup> studied the flow sources associated with surface pressure events in a turbulent boundary layer. Interestingly, these authors showed that the extent to which the inclusion of a quadratic or higher order term is necessary, strongly depends on the shape of the joint probability density function (JPDF) between the conditional and unconditional events. In particular, if the JPDF is Gaussian, then the linear estimate may be sufficient to capture the relation between the two events. However, if this is not the case, a higher order may be recommended.<sup>8</sup> Pressure as the unconditional source was also used successfully by Garcia-Sagrado and Hynes<sup>16</sup> to study the coherent structures associated with wall-pressure fluctuations in the trailing edge region of an airfoil. Related applications which use pressure-based estimation include the study of vortical structures and of the associated pressure fluctuations in the surrounding of a subsonic round jet.<sup>29</sup>

Wall-pressure based stochastic estimation techniques were successfully applied to obtain estimates of the velocity field in cavity flows, e.g., Murray and Ukeiley,<sup>26</sup> Ukeiley and Murray,<sup>37</sup> and Zhang and Naguib.<sup>39</sup> In particular, Ukeiley and Murray,<sup>37</sup> successfully applied the QSE and showed it to be an effective tool for the representation of the time-dependent phenomena of the velocity field. Zhang and Naguib<sup>39</sup> studied the evolution of the coherent structures generating the pressure oscillations in a cavity, by using arrays of electret condenser microphones. Interestingly, the author reported no significant improvement when the quadratic estimate was used.

Stochastic estimation techniques have been frequently applied together with low dimensional modeling techniques, such as the proper orthogonal decomposition (POD; Berkooz *et al.*<sup>5</sup>). The LSE-POD complementary technique, introduced by Bonnet *et al.*,<sup>7</sup> allows the estimation of the temporal dependence of the first POD coefficients, providing a temporally resolved low dimensional estimate of the flow state. One advantage of the approach is that POD coefficients are scalar quantities which are independent from the spatial location. This reduces the amount of coefficients necessary to estimate the whole flow field.<sup>26</sup> Examples of applications of this technique to gain insight into the temporal dynamics of unsteady flows are copious in the literature, e.g., Murray and Ukeiley<sup>26</sup> for cavity flow, Hudy *et al.*<sup>21</sup> for a back-facing step flow, and Iqbal and Thomas<sup>22</sup> for a turbulent jet.

An important application of stochastic estimation techniques is that of real-time flow control, where accurate estimates of the flow field must be available as input in order for the control scheme to be effective.<sup>26</sup> Stochastic estimation – POD complementary techniques have been widely used for this goal to provide an instantaneous, low dimensional representation of the flow state. Pinier *et al.*<sup>30</sup> experimentally implemented an efficient closed-loop feedback control using such techniques to delay flow separation over a NACA-4412 airfoil equipped with leading-edge zero-net-mass-flux actuators.

Although it has been successfully used in several applications, some aspects of the classical stochastic estimation technique could be improved. Cattafesta *et al.*<sup>10</sup> termed this technique a “static estimator” since it uses only one sample of the unconditional source to estimate the flow state, resulting in a *single-time-delay* technique (STD). Because of this reason, the classical stochastic estimation technique is not a robust estimation tool as it is affected by the presence of background uncorrelated fluctuations which deteriorate its accuracy. To cope with this problem, several sensors are needed to obtain estimates of good quality (Garcia-Sagrado and Hynes,<sup>16</sup> Zhang and Naguib,<sup>39</sup> and Murray and Ukeiley<sup>26</sup>), even in the case of the quadratic estimate. By contrast *dynamic* estimators or observers can be more accurate in reproducing the complex dynamics of an unsteady flow.

Rowley *et al.*,<sup>33</sup> used a Kalman filter based dynamic observer to estimate the state of a cavity flow from noisy pressure measurements, and observed better performance with respect to the classical LSE technique.

Another drawback of the single-time-delay approach is that occurring for the case when the conditional and unconditional sources are separated by a time lag due to a convection speed. Naguib *et al.*<sup>27</sup> embedded such time lag information in the estimate but for the single-time-delay estimate such a lag must be known, for example, from cross-correlation analysis. To overcome this problem, two approaches have been proposed. One approach is the so-called spectral linear stochastic estimation (SLSE), proposed by Ewing and Citriniti<sup>15</sup> to study an annular mixing layer flow, treated in detail by Tinney *et al.*<sup>35</sup> Such approach consists in estimating the conditional event in the frequency domain and for this reason, for the case where there is a separation in time between the events, the time lag is embedded in the spectral estimator. Furthermore, with this approach only those frequency components for which the coherence spectrum between the conditional and unconditional sources is high enough, and larger than a chosen threshold, are retained. The other components, for which poor correlation exists, are suppressed by setting the coefficients corresponding to these frequencies to zero. Tinney *et al.*<sup>35</sup> observed that such an approach is necessary when the conditional and unconditional sources have significantly different spectral characteristics or when they are of different physical quantities.

Another approach which can overcome the time lag issue was proposed by Durgesh and Naughton<sup>14</sup> and is a *multi-time-delay* LSE-POD complementary technique. The approach developed by these authors consisted in using a given number of past and future measurements of the pressure signal to estimate the time evolution of the first POD mode coefficients. This provided a low dimensional, time-resolved reconstruction of the flow field at a given time instant. The authors applied this approach to a bluff body near wake, which was investigated by Particle Image Velocimetry and wall-pressure measurements. The authors reported that the multi-time-delay approach (MTD) was successful in capturing the dynamics of the wake and showed a significant improvement in accuracy of the estimate with respect to the classical *single-time-delay* stochastic estimation technique. The authors also highlighted that the multiple time-delays must be optimized to match the correlation peaks, in order to achieve best results.

The idea of using multiple past measurements for obtaining more accurate estimates was introduced by Ukeiley *et al.*,<sup>38</sup> which introduced dynamic stochastic estimation as a mean to obtain predictions of future values of the wall-pressure from multiple past values of the same wall-pressure time history. These authors introduced auto-regressive and auto-regressive moving average approaches, commonly used in system identification of dynamic systems, and found that it was possible to accurately describe the time evolution of the wall-pressure.

Despite the seminal new ideas of Ukeiley *et al.*<sup>38</sup> and the work of Durgesh and Naughton,<sup>14</sup> several aspects of the MTD-LSE approach need to be further investigated and detailed. First, a thorough analytic derivation of the method, which outlines its fundamental properties, needs to be reported with an emphasis on fluid dynamics aspects. In particular, it is necessary to thoroughly describe the spectral properties of the estimated flow field and to focus on the residual error of the estimate, how it is composed and which are its sources. Furthermore, a critical comparison of the MTD-LSE approach with single-time-delay techniques, whether linear or high-order, is needed to fully appreciate the effectiveness and the convenience of the MTD approach, in particular, with a strong focus on the number of past values used. In this regard, a full explanation of the reasons why the MTD approach is preferable is required, with an emphasis on both control applications and as a tool to obtain physical insight in complex flows. Finally, an analysis on the effects of using more than one sensor and of its location in the flow field is required to provide a practical rule of thumb for positioning the flow sensors in flow control applications.

All these aspects need to be detailed to fully advance the state-of-the-art of flow estimation techniques. In this paper, we address all of them and, as a demonstration, we apply the method to the estimation of the spatio-temporal dynamics of the velocity fluctuations in a shear layer developing over a curvilinear unconventional cavity. This is performed by using wall-pressure measurements from multiple sensors mounted inside the cavity.

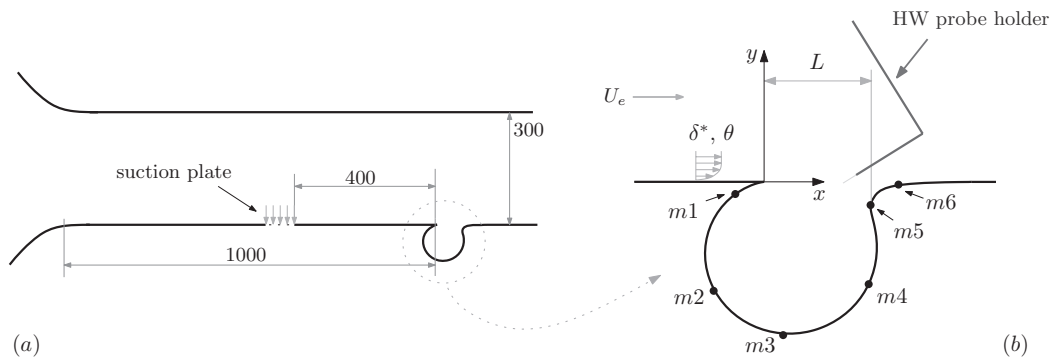


FIG. 1. Sketches of the test section setup (a), and of the cavity geometry (b). The suction plate is located about  $6L$  upstream of the cavity cusp, the leading edge. The locations of the six microphones, 30 mm away from the center-line section, are also shown in part (b).

In Sec. II, the experimental setup is presented. Section III is devoted to the mathematical treatment of the technique, while Sec. IV is dedicated to presenting the results of the application of the technique.

## II. EXPERIMENTAL SETUP

### A. Test section arrangement and cavity model

The experiment was conducted in an open-circuit type wind tunnel. The test section has width, height, and length of 720, 300, and 3600 mm, respectively. Maximum speed in this wind tunnel was about 25 m/s. The flow investigated developed in a cavity with a curvilinear geometry located on the bottom surface of the wind tunnel test section, as shown in Figure 1(a). The flow in such curvilinear geometries have been recently investigated by several authors, e.g., Lasagna *et al.*,<sup>23</sup> Olsman *et al.*,<sup>28</sup> Hokpunna and Manhart,<sup>20</sup> and Donelli *et al.*,<sup>13</sup> because of the interest in controlling flows past a thick airfoil which trap a vortex in one of such cavities located on its upper surface. The shape of the present cavity is the same used by Hokpunna and Manhart.<sup>20</sup> The cavity had a nominal opening length equal to  $L = 68$  mm and a span of 420 mm, so that the aspect ratio was about 6.6. The cavity spanned 58% of the test section width, leaving a free space of 150 mm between the cavity ends and the vertical test section walls. This prevented interactions between the corner flows developing at the angles of the test section with the cavity flow. The cavity was designed using a rib-like structure, and its surface was made of 0.5 mm-thick poly-carbonate film. Figure 2(a) shows a drawing of the cavity model. The thickness of the film was chosen to be as large as the manufacturing process allowed, in order to prevent fluid-structure coupling induced by the fluid oscillations that were expected. The

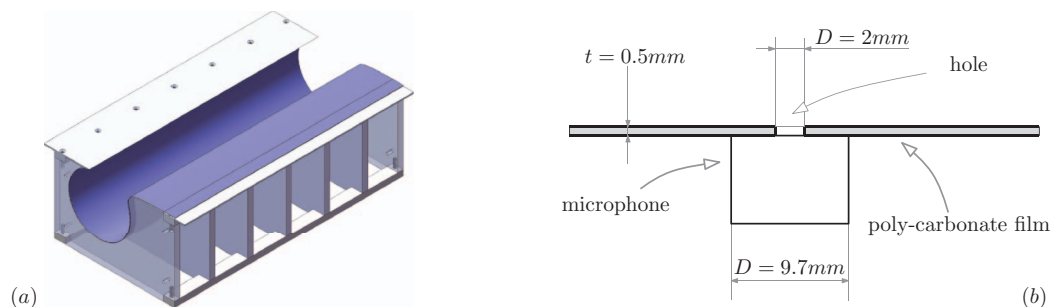


FIG. 2. Drawing of the rib-like structure of the cavity model (a), and sketch of the mounting of microphone under the poly-carbonate film (b).

cavity was then embedded in the bottom surface of the test section, at a distance of about 1.0 m from the upstream contraction section.

A 120 mm long perforated plate spanning the entire test section width was located 400 mm upstream of the cavity leading edge as depicted in Figure 1(a). Suction through this plate allowed the variation of the boundary layer properties at the cavity cusp. Great care was taken to ensure that uniform suction was applied along the plate, in order to ensure characteristics of the incoming boundary layer across the whole cavity span. This was achieved using *ad hoc* dividing vanes in the drawer below the plate.

## B. Velocity measurements

Extensive velocity measurements were performed using constant temperature hot wire anemometry. An A.A. LabSystems AN1003 anemometer with a built-in signal conditioning unit was used to measure the velocity component normal to sensor. A single-wire probe, (length 0.9 mm and diameter 5  $\mu\text{m}$ ), was used. The probe was frequently calibrated *in situ* in the middle of the vein and at a sufficient distance upstream of the cavity to render negligible its influence.

To reduce interference effects generated by the probe holder on the shear layer flow, this was tilted by 40° for both the calibration and the measurements, as shown in Figure 1(b). The probe holder was fixed to a motorized two-axis traverse system located on the top of the test section. A LabVIEW interface provided completely automated traversing and data-acquisition in  $x - y$  planes.

The cavity shear layer was preliminarily investigated in several spanwise sections to assess its 2D properties. The second order statistics of the shear layer flow were reasonably constant in 90% of the span with minor deviations at the ends. Therefore, more detailed measurements were subsequently conducted in the centerline section only. Velocity profiles across the shear layer thickness were measured at 46 locations along the  $x$  axis. For each profile, 34 points were opportunely distributed across the shear layer thickness in the range  $-4\delta < y < 4\delta$  ( $\delta$  is the 99% boundary layer thickness at the cavity leading edge), concentrating the points in regions of stronger variations of the flow properties. Furthermore, in order to correctly resolve the spatio-temporal dynamics of the estimated velocities in the shear layer, as will be detailed later, the profiles were distributed along the  $x$  axis with variable spacing, namely, 5 mm in the first third of the cavity length, 2 mm in the second third, and 1 mm in the last.

## C. Pressure fluctuations measurements

Pressure fluctuations measurements were performed using high-sensitivity electret condenser microphones, of a similar type as those used by other authors, e.g., Zhang and Naguib,<sup>39</sup> Garcia-Sagrado and Hynes.<sup>16</sup> The microphones, with a diameter and height of 9.7 and 6 mm, respectively, were powered by a dedicated power supply unit through custom-made RC circuits. These microphones, which only measure the fluctuating component, were positioned under the poly-carbonate film of the cavity, and aligned with a 2 mm hole as shown in Figure 2(b). The large diameter of the hole was chosen as a compromise between the need to maximize the signal to noise ratio and minimization of spatial filtering effects.

Six microphones were located in a section of the cavity 30 mm away from the mid-span as shown in Figure 1. This position was chosen to prevent the influence of the probe holder wake on the measurements of the pressure fluctuation if the microphones were located in the central section. The absence of any interference was ensured by verifying that the pressure spectra measured with and without the probe holder in flow were equal. Five other microphones were located transversely along the downstream shoulder of the cavity in the same position of microphone  $m5$  with a spacing of 60 mm, but results concerning these are not presented here.

The dynamic properties of the microphones were estimated by an *ad hoc* calibration similar to that performed by Zhang and Naguib<sup>39</sup> and Garcia-Sagrado and Hynes.<sup>16</sup> The objective of the calibration was to find the microphone transfer function  $H(f)$ . These dynamic properties are summarized in terms of gain in mV/Pa and phase delay, as a function of the frequency. The calibration setup consisted of a flat plate located at a distance of 50 cm in front of a high power

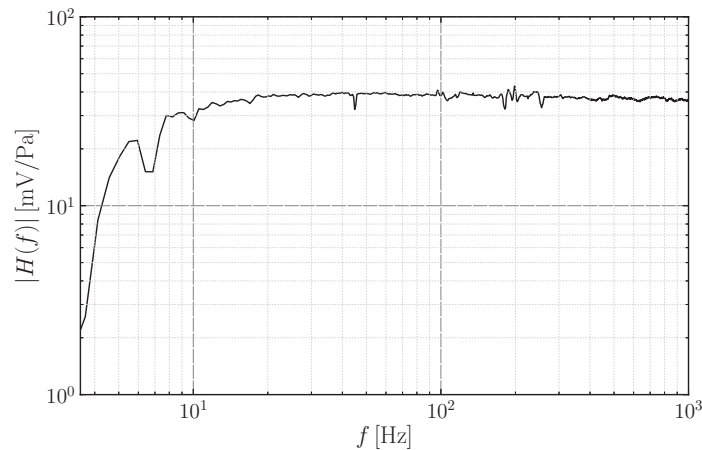


FIG. 3. Typical amplitude response of an electret condenser microphone.

loudspeaker, which produced a fluctuating pressure field on the plate. The electret microphones were positioned on this plate with the same arrangement of the measurements described above. A reference high-precision microphone was flush-mounted in the center of the plate. This was a high quality 1/4 in. Brüel&Kjær (B&K) (type 4939) condenser microphone. This microphone has pre-amplification, flat frequency response in the range 10–10 000 Hz and selectable gain by means of a dedicated power-supply/signal conditioning unit.

The microphones calibration was performed according to system identification procedures, described in detail by Ljung.<sup>24</sup> A zero-mean Gaussian noise, pass-band filtered between 2 and 2500 Hz, was fed to the loudspeaker through an amplifier. Because the loudspeaker signal values were sampled from a Gaussian distribution, large values exceeding the input capability of the loudspeaker could occur. For this reason the signal was clipped between  $\pm e_{th}$ , a chosen threshold voltage. However, since clipping the signal in the time domain affects the signal spectrum in the frequency domain, the clipping and bandpass filtering were repeatedly applied to the signal, until it reached satisfactory time and frequency domain characteristics.

Simultaneous measurements from the electret and the B&K microphone were sampled at a frequency of 10 kHz and for 120 s. The length of the time histories was such as to provide satisfactory convergence of the spectral characteristics of the signals. Transfer function estimates, evaluated according to Bendat and Piersol,<sup>4</sup> were then obtained as

$$H(f) = \frac{\Phi_{Bm}(f)}{\Phi_{BB}(f)}, \quad (1)$$

where  $\Phi_{Bm}(f)$  is the cross-spectral density between the voltage signal of the electret microphone and the pressure signal of the B&K microphone, while  $\Phi_{BB}(f)$  is the power-spectral density of the B&K microphone signal. All the spectral densities were obtained via the Welch algorithm, to improve the quality of the spectral density estimate.

Amplitude and phase response plots were analyzed in detail for each microphone under test. Figure 3 shows a typical amplitude response plot. As expected, the microphones significantly attenuated low-range frequency components below 10 Hz. The gain of each microphone was found to be sufficiently constant in the band 20–1000 Hz, in which most of the shear layer dynamics were expected, and was practically constant in successive calibration experiments. The phase shift introduced by the microphone was found to be negligible, of the order of 50  $\mu$ s in the frequency range of interest. For this reason, it was not taken into account in the subsequent analyses. Furthermore, resonance effects due to the arrangement were not observed. Finally, in order to test the linearity properties of the microphones, different calibration experiments with different amplitude of the loudspeaker driving signal were performed. Linear behavior was observed for a range of pressure amplitudes much larger than those expected in the cavity flow.

During the cavity flow experiments, velocity and wall-pressure time histories of  $2^{17}$  samples were simultaneously sampled at 8 kHz by 24 bit resolution National-Instruments 9239 data acquisition modules, mounted on a NI cDAQ 9172 chassis. These units have a built-in anti-aliasing filter set at 46% of the sampling frequency. The size of the time histories was chosen in order to guarantee convergence of the second order statistics for both the velocity and wall-pressure.

### III. MULTI-TIME-DELAY LINEAR STOCHASTIC ESTIMATION APPROACH

The LSE technique was introduced by Adrian<sup>1</sup> as a means to approximate the conditional average of the fluctuating velocity vector field given the occurrence of an event vector  $\mathbf{E}$ . This conditional average is defined as

$$\hat{\mathbf{u}}(\mathbf{x}, t) = \langle \mathbf{u}(\mathbf{x}, t) | \mathbf{E} \rangle \quad (2)$$

and can be expanded in a Taylor series of the event. In general,  $\mathbf{u}$  indicates the velocity fluctuation, since the mean flow is known and does not need to be estimated.<sup>8</sup>

As demonstrated by several authors, e.g., Picard and Delville,<sup>29</sup> Naguib *et al.*,<sup>27</sup> and Ukeiley and Murray,<sup>37</sup> the event can be also obtained from wall-mounted pressure sensors. For the single sensor case, the event reads as

$$\mathbf{E} = \{p_e < p(t) < p_e + dp\} \quad (3)$$

and confines the wall-pressure into a small window between  $p_e$  and  $p_e + dp$ . The linearly truncated Taylor expansion of the conditional average then reads as

$$\hat{\mathbf{u}}(\mathbf{x}, t) = \mathbf{a}(\mathbf{x})p(t) \quad (4)$$

and the coefficients  $\mathbf{a}(\mathbf{x})$  are obtained from unconditional statistics, i.e., two point correlations, which result from a minimum square error procedure, fully described in Guezennec.<sup>18</sup> This is a *single-time-delay* approach, in that the event vector  $\mathbf{E}$  specifies a condition on the wall-pressure only at a single time instant. This time instant can be the present time  $t$  or can refer to a past time  $t - \tau$ , as shown, for example, by Naguib *et al.*<sup>27</sup> The technique can then be used to reconstruct the time-resolved dynamics of the conditional flow field, based on wall-pressure measurements.

The basic idea of the *multi-time-delay* approach is that in order to obtain a more accurate time resolved reconstruction of the flow field  $\hat{\mathbf{u}}(\mathbf{x}, t)$  at time  $t$ , multiple past wall-pressure samples should be taken into account. Only past samples are considered here, since this would be the natural approach to take in a real-time flow control scheme. For the single sensor case, this corresponds to defining an event vector  $\mathbf{E}$  of the form

$$\mathbf{E} = \{p_{e_0} < p(t) < p_{e_0} + dp, p_{e_1} < p(t - \Delta t) < p_{e_1} + dp, \dots, p_{e_n} < p(t - n\Delta t) < p_{e_n} + dp\}, \quad (5)$$

which is made up of  $n + 1$  simultaneous conditions on the past values of the wall-pressure time history. This event vector can also be naturally extended to contain past samples from multiple sensors, defining a *multi-point*, multi-time-delay stochastic estimation technique. The motivation for specifying such an event vector derives from the observation that this expanded event imposes a *dynamic* condition on the average of the flow field, which may provide a more detailed description of the temporal evolution of the flow. On the other hand, specifying only a single-time-delay condition, whether from single or multiple sensors, is an incomplete description of the dynamic state of the flow and corresponds to an average over all the possible dynamic flow states.

Given these considerations, the linearly truncated expansion of the conditional average (2), using the event of Eq. (5) and including multiple sensors, can be written as

$$\hat{\mathbf{u}}(\mathbf{x}, t) = \sum_{j=1}^M \sum_{k=0}^n \mathbf{b}_{kj}(\mathbf{x})p_j(t - k\Delta t). \quad (6)$$

The first summation is done over the  $M$  available wall-pressure sensors, while the second is done over the  $n + 1$  samples of the wall-pressure time history. We call  $n$  the model order. It is immediately apparent that the case  $n = 0$  and  $M = 1$  corresponds exactly to the definition of the single-point,

single-time-delay linear stochastic estimation of Eq. (4). In this paper, only the linearly truncated expansion is considered and treated, but extensions to higher order terms may also be developed.

The problem of finding the coefficients  $\mathbf{b}_{kj}(\mathbf{x})$  is solved in the same way as for single-time-delay estimates, as described by Guezennec,<sup>18</sup> by choosing the values of  $\mathbf{b}_{kj}(\mathbf{x})$  which provide a minimum mean-square estimation error. However, for a multi-time-delay approach there are some fundamental differences, briefly reviewed here in the following. For a more thorough description of the least square method the reader is referred to Ljung.<sup>24</sup>

### A. Single-point, multi-time-delay linear stochastic estimation

We first consider the problem of single-point estimates,  $M = 1$ , leaving the different details specific to the multi-point approach, ( $M > 1$ ), to Sec. III B. Furthermore, the problem of estimating only one of the velocity components at a given point  $\mathbf{x}_0$  is treated. This is, in fact, the “base” problem, independently repeated over all the spatial locations and for all the available velocity components.

From simultaneous measurements of the velocity fluctuation  $u(t)$  at point  $\mathbf{x}_0$  and of the wall-pressure  $p(t)$ , statistically significant collections of  $N$  samples are extracted:  $\{u(i)\}$ ,  $\{p(i)\}$   $i = 1, \dots, N$ , where  $p(i) = p(i\Delta t)$ , with  $\Delta t$  being the sampling interval. Introducing a matrix notation, Eq. (6) may be rewritten as

$$\hat{u}(i) = \boldsymbol{\varphi}(i)^T \boldsymbol{\theta}, \quad (7)$$

where  $\boldsymbol{\varphi}(i) = [p(i) p(i-1) \dots p(i-n)]^T$  is called the regressors vector at time instant  $i$  and  $\boldsymbol{\theta} = [b_0 b_1 \dots b_n]^T$  is the vector of the unknown coefficients. These two vectors have size  $(n+1) \times 1$ . Furthermore, since data are not available for  $i < 0$ , the first full regressors vector can be obtained at  $i = n-1$ .

The unknown coefficients vector is found as the minimizing argument of the mean-square estimation error defined as

$$\begin{aligned} E(\boldsymbol{\theta}) &= \frac{1}{N-n} \sum_{i=n-1}^N [u(i) - \hat{u}(i)]^2 = \frac{1}{N-n} \sum_{i=n-1}^N [u(i) - \boldsymbol{\varphi}(i)^T \boldsymbol{\theta}]^2 \\ &= \frac{1}{N-n} \sum_{i=n-1}^N \left[ u(i) - \sum_{k=0}^n b_k p(i-k) \right]^2, \end{aligned} \quad (8)$$

and it is obtained by differentiating Eq. (8) with respect to  $\boldsymbol{\theta}$  and setting to zero, which yields a set of linear equations called the *normal equations*

$$\left[ \frac{1}{N-n} \sum_{i=n}^N \boldsymbol{\varphi}(i) \boldsymbol{\varphi}^T(i) \right] \boldsymbol{\theta} = \frac{1}{N-n} \sum_{i=n}^N \boldsymbol{\varphi}(i) u(i), \quad (9)$$

compactly written as

$$\mathbf{R} \boldsymbol{\theta} = \mathbf{f}. \quad (10)$$

The matrix  $\mathbf{R}$  has a particular structure which allows the computation of its elements in a fast and convenient way. It is straightforward to see that

$$\mathbf{R} = \frac{1}{N-n} \sum_{i=n}^N \begin{bmatrix} p_i p_i & p_{i-1} p_i & \dots & p_{i-n} p_i \\ p_{i-1} p_i & p_{i-2} p_i & \dots & p_{i-n} p_{i-1} \\ \vdots & \vdots & \ddots & \vdots \\ p_{i-n} p_i & p_{i-n} p_{i-1} & \dots & p_{i-n} p_{i-n} \end{bmatrix}, \quad (11)$$

where  $p_i = p(i)$ . This means that

$$\mathbf{R}_{ij} = r_{pp}(\kappa), \quad \kappa = j - i, \quad (12)$$

where  $r_{pp}(\kappa)$  is the auto-correlation function of the pressure signal, defined as

$$r_{pp}(\kappa) = \overline{p(i)p(i+\kappa)}. \quad (13)$$

The matrix  $\mathbf{R}$  is thus a Toeplitz matrix with size  $(n + 1) \times (n + 1)$ , which can be formed from the auto-correlation function of the pressure signal, and reads as

$$\mathbf{R} = \begin{bmatrix} r_{pp}(0) & r_{pp}(1) & \dots & r_{pp}(n) \\ r_{pp}(1) & r_{pp}(0) & \dots & r_{pp}(n-1) \\ \vdots & \vdots & \ddots & \vdots \\ r_{pp}(n) & r_{pp}(n-1) & \dots & r_{pp}(0) \end{bmatrix}. \quad (14)$$

The column vector  $\mathbf{f}$ , of size  $(n + 1) \times 1$ , can be obtained in a similar way, by considering that

$$\mathbf{f} = \frac{1}{N-n} \sum_{i=n}^N \begin{bmatrix} p_i \\ p_{i-1} \\ \vdots \\ p_{i-n} \end{bmatrix} u(i) = \begin{bmatrix} r_{pu}(0) \\ r_{pu}(1) \\ \vdots \\ r_{pu}(n) \end{bmatrix}, \quad (15)$$

where we have introduced the cross-correlation function between the pressure and the velocity  $r_{pu}(\kappa) = \overline{p(i)u(i+\kappa)}$ .

The matrices  $\mathbf{R}$  and  $\mathbf{f}$  can thus be constructed from the auto- and cross-correlation functions of the wall-pressure and velocity measurements. The computational time required for obtaining these matrices can be significantly reduced by exploiting the correlation theorem and using fast Fourier transform techniques to obtain the correlation function. Then the unknown coefficients vector can be obtained by solving the linear system  $\mathbf{R}\boldsymbol{\theta} = \mathbf{f}$ .

## B. Multi-point multi-time-delay stochastic estimation

For a multi-point estimate with  $M > 1$  sensors, the procedure described above is still valid, but there are some small differences, detailed here. The regressors vector in Eq. (7) becomes a column vector of  $M(n + 1) \times 1$  elements which reads as

$$\boldsymbol{\varphi}(i) = [p_1(i), p_1(i-1), \dots, p_1(i-n), p_2(i), p_2(i-1), \dots, p_2(i-n), \dots, p_M(i), p_M(i-1), \dots, p_M(i-n)]^T, \quad (16)$$

and contains past values of the  $M$  wall-pressure time histories. Similarly, the unknown coefficients vector  $\boldsymbol{\theta}$  reads as

$$\boldsymbol{\theta} = [b_{10}, \dots, b_{1n}, b_{20}, \dots, b_{2n}, \dots, b_{M0}, b_{M1}, \dots, b_{Mn}]^T. \quad (17)$$

The matrix  $\mathbf{R}$  from the normal Eq. (10) is derived in the same way as before, but it is now a symmetric block matrix, composed of  $M \times M$  blocks of size  $(n + 1) \times (n + 1)$ . Each block is a Toeplitz matrix made up of auto- or cross-correlation values between the wall-pressure sensors. The matrix has the form

$$\mathbf{R} = \begin{bmatrix} \mathcal{R}_{p_1 p_1} & \mathcal{R}_{p_1 p_2} & \dots & \mathcal{R}_{p_1 p_M} \\ \mathcal{R}_{p_2 p_1} & \mathcal{R}_{p_2 p_2} & \dots & \mathcal{R}_{p_2 p_M} \\ \vdots & \vdots & \ddots & \vdots \\ \mathcal{R}_{p_M p_1} & \mathcal{R}_{p_M p_2} & \dots & \mathcal{R}_{p_M p_M} \end{bmatrix}, \quad (18)$$

where the  $i$ th,  $j$ th block  $\mathcal{R}_{p_i p_j}$ , is such that

$$\mathcal{R}_{p_i p_j} = \begin{bmatrix} r_{p_i p_j}(0) & r_{p_i p_j}(1) & \dots & r_{p_i p_j}(n) \\ r_{p_i p_j}(1) & r_{p_i p_j}(0) & \dots & r_{p_i p_j}(n-1) \\ \vdots & \vdots & \ddots & \vdots \\ r_{p_i p_j}(n) & r_{p_i p_j}(n-1) & \dots & r_{p_i p_j}(0) \end{bmatrix} \quad (19)$$

with  $r_{p_i p_j}(\kappa)$  being the cross-correlation function between the  $i$ th and  $j$ th sensors signals.

In a similar way, the column vector  $\mathbf{f}$  from the normal equations, Eq. (10), becomes

$$\mathbf{f} = \begin{bmatrix} \mathcal{R}_{p_1u} \\ \mathcal{R}_{p_2u} \\ \vdots \\ \mathcal{R}_{p_Mu} \end{bmatrix}, \quad (20)$$

where each of the  $M$  blocks  $\mathcal{R}_{p_iu}$  is a  $(n + 1) \times 1$  column vector composed of the values of the cross-correlation function  $r_{p_iu}(k)$  between pressure and velocity for  $k = 0, \dots, n$ . The linear system  $\mathbf{R}\boldsymbol{\theta} = \mathbf{f}$  can then be solved for each spatial location and for each velocity component, yielding the full set of coefficients  $\mathbf{b}_{kj}(\mathbf{x})$ . With these and from new wall-pressure measurements the spatio-temporal evolution of the flow can be estimated, using Eq. (6).

#### IV. RESULTS

Some basic results concerning the cavity flow investigated are shown first in this section, which discusses the mean flow properties and the spectral characteristics of the velocity and wall-pressure. This introduces the results of the application of the multi-time-delay stochastic estimation approach, shown in detail in Secs. IV B and IV D, for the single- and multi-point approaches, respectively.

##### A. Mean flow and spectral analysis

The test conditions treated in this paper refer to a free-stream velocity equal to  $U_e = 5.80$  m/s, at which the Reynolds number based on the cavity length  $L = 68$  mm is equal to  $Re_L = LU_e/\nu = 2.77 \times 10^4$ . The level of suction operated on the perforated plate upstream of the cavity is sufficient to produce a laminar boundary layer at the cavity leading edge. In fact, the velocity profile, measured in  $x = -10$  mm, reported in Figure 4, shows good agreement with a least-squares fit of the Blasius laminar solution. The profile has a shape factor  $H = \delta_0^*/\theta_0 = 2.19$ , where  $\delta_0^* = 1.32$  mm (displacement thickness), and  $\theta_0 = 0.60$  mm (momentum thickness). The boundary thickness  $\delta_0$  is taken to be equal to 4.4 mm. With such a boundary layer the ratio  $L/\theta_0$  is equal to 113.

Figure 5 depicts the streamwise evolution of the mean velocity profile in four selected locations. The velocity profile at  $x/L = 0.01$  quickly changes from the boundary layer profile of Figure 4 to a shear-layer-like profile. The profiles clearly evidence the thickening of the shear layer as it develops downstream. In particular, the spreading of the shear layer occurs towards the interior of the cavity.

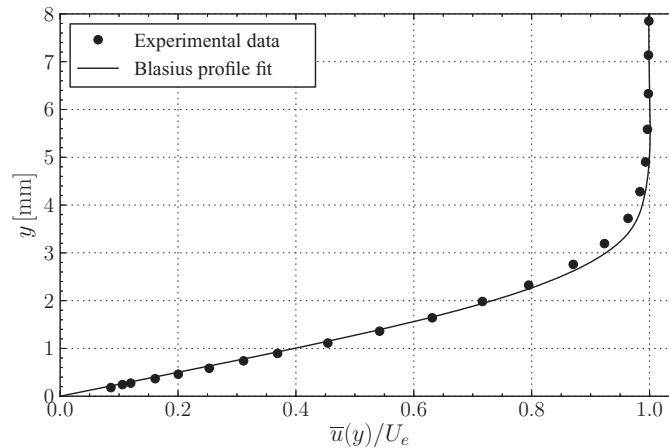


FIG. 4. Mean velocity  $\bar{u}(y)/U_e$  boundary layer profile at  $x = -10$  mm. Experimental data and a Blasius solution fit are depicted.

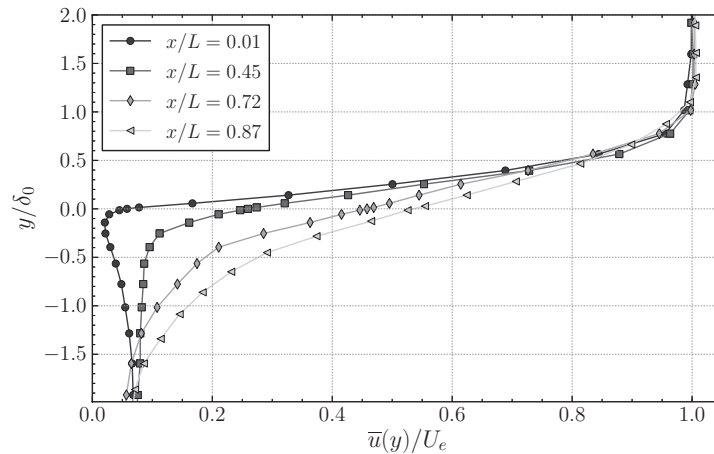


FIG. 5. Mean velocity profiles  $\bar{u}(y)/U_e$  at selected streamwise positions in the shear layer.

This indicates that the locus of the points  $y$  where  $\bar{u}/U_e = 0.5$  is deviated towards the inner region of the shear layer, as found by Gharib and Roshko<sup>17</sup> and Sarohia.<sup>34</sup>

Figure 6 shows a contour map of the non-dimensional root-mean-square value of the velocity fluctuation  $u'_{rms}/U_e$ . The cavity cusp is located in the origin, and the downstream part of the cavity is shown on the lower right part of the figure. The flow is from left to right. The most intense fluctuations are observed in the impingement region, where the coherent structures developing in the shear layer break up into small scale structures. This was also highlighted by smoke flow visualizations, not reported here.

High levels of fluctuations can also be observed in the shear layer, especially for  $x/L > 0.5$ . In fact, the amplitude of the velocity fluctuations grows as the shear layer develops downstream. Although not shown here, the velocity fluctuations show a strong initial exponential growth up to about  $0.5L$ , as also reported by several authors, e.g., Gharib and Roshko.<sup>17</sup> From the figure, it is evident that  $u'_{rms}/U_e$  reaches a peak in  $x/L = 0.6$ , followed by an enlargement of the region intense fluctuations. Here, the largest part of the energy is due to the coherent oscillations due to Kelvin-Helmholtz instability, a characteristic of cavity flows in the shear-layer mode (Rowley *et al.*<sup>32</sup>), where strong coupling between velocity and pressure takes place.

This coupling was preliminary investigated at different wind tunnel speeds. A wall-pressure time history was measured with each microphone at 55 velocities from 2 to 10 m/s and a power

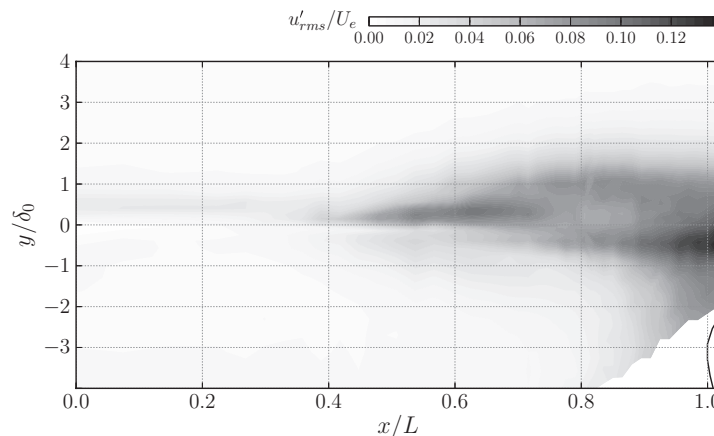


FIG. 6. Contour map of the normalized root mean-square value of the velocity fluctuation  $u'_{rms}/U_e$ , across the whole cavity shear layer. The cusp is set at the origin, flow is from left to right.

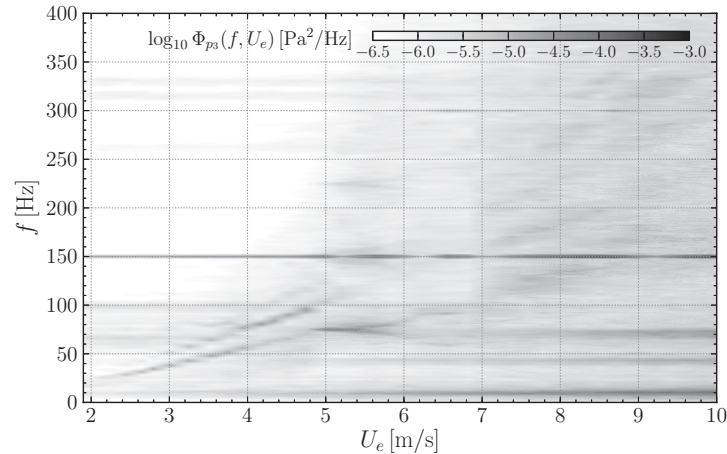


FIG. 7. Velocity-frequency spectrogram of the wall-pressure time history from microphone *m6*. The contour map shows the base ten logarithm of the power spectral density of the wall-pressure signal.

spectrum was computed for each of these. Results in the form of a velocity-frequency spectrogram are shown in Figure 7 for microphone *m6*, which better highlights the characteristics of the wall-pressure fluctuations of the shear layer flow. In the range of velocities between 2 and 5 m/s, and for frequencies between 0 and 100 Hz, three different narrow energy concentration bands can clearly be observed. These bands correspond to the second, third, and fourth natural instability modes of the shear layer. Their frequencies can be predicted using the Rossiter equation, Rossiter,<sup>31</sup> which reads as

$$f_n = \frac{U_e}{L} \frac{n - \alpha}{M + 1/k}, \quad (21)$$

where  $f_n$  is the frequency of the  $n$ th mode,  $\alpha$  is a parameter which takes into account the phase lag between the impingement of a coherent structure and the production of an acoustic wave,  $k$  defines the ratio of the phase velocity of the convective disturbances in the shear layer to the external velocity, while  $M$  is the freestream Mach number. Good correlation between the experimental results and the Rossiter equation are found by setting the phase lag  $\alpha$  equal to zero, as it is commonly observed in low Mach number flows (Cattafesta *et al.*<sup>9</sup>), and an average value of  $k$  approximately equal to 0.5. Interestingly, the first shear layer mode cannot be observed. The signature of these modes can barely be detected for velocities larger than 7 m/s, for which the incoming boundary layer is fully turbulent. Furthermore, the slope of the bands appears to increase as  $U_e$  increases, which means that  $k$  slightly increased with the external velocity. This is probably due to the variation of the boundary layer properties as the wind tunnel speed is increased.

The spectrogram is also characterized by high energy concentrated at a frequency of  $f = f_{wt} = 150$  Hz, for all the velocities tested. This frequency has been identified as due to a wind tunnel acoustic resonance (AGARD-AR-336<sup>3</sup>), which originated in the settling chamber of the wind tunnel. The presence of this resonance was previously found in pressure fluctuation measurements in the test section without the cavity installed.

There is a complex interaction between the wind tunnel acoustic resonance and the natural instability modes. At velocities where the frequencies of natural instability modes of the shear layer are close to  $f_{wt}$ , the shear layer locks in to the forcing frequency. This condition is evidenced as a strong increase of the wall-pressure fluctuations energy at the resonance frequency. This phenomenon is evident at speeds equal to 5.6, 6.5, and 8.4, where lock-in between the fourth, third and second natural shear layer mode occurs, respectively. Similar interactions with the wind tunnel acoustic modes were also observed by Chatellier *et al.*<sup>11</sup> and Olsman *et al.*<sup>28</sup>

Lock-in conditions also occur at non-integer frequencies of the wind tunnel resonance mode. At  $U_e = 5$  m/s, the second shear layer mode locks in to the first sub-harmonic of the wind tunnel acoustic resonance for  $f = f_{wt}/2 = 75$  Hz. At slightly higher velocities, two energy bands bifurcate

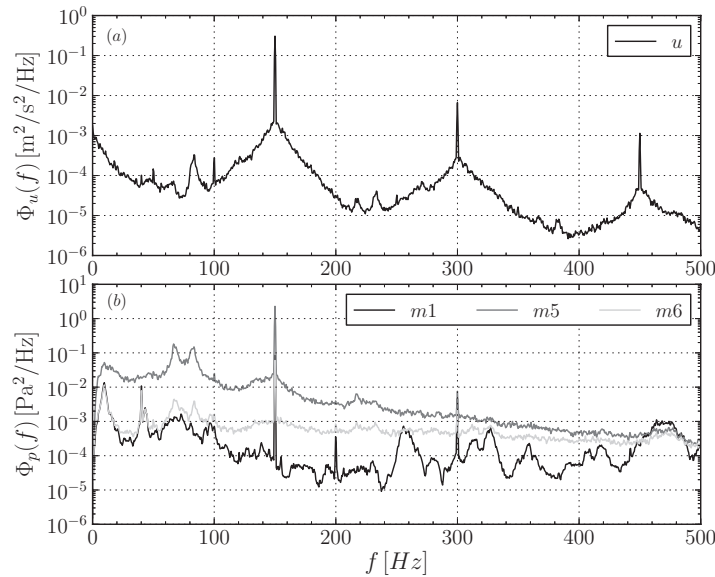


FIG. 8. Power spectral densities of the velocity signal at point  $P$  in  $x/L = 0.6$ ,  $y/\delta = 0.34$  (a), and of the wall-pressure signals for microphones  $m1$ ,  $m5$ ,  $m6$  (b).

symmetrically with respect to this frequency. A similar interaction, but with lesser intensity, develops at this same velocity for a frequency equal to  $f = 3/2 f_{wt}$ .

The test conditions treated in this paper refer to  $U_e = 5.8$  m/s, a velocity slightly higher than that at which lock-in of the third mode occurs. For the purpose of the paper, the presence of the interaction between the wind tunnel acoustic resonance and the shear layer oscillation is unimportant, since the basic concepts discussed have general validity.

Figure 8(a) shows power spectral densities for the velocity time history in the point in the shear layer where the most intense fluctuations have been observed, namely, at  $x/L = 0.6$  and  $y/\delta = 0.34$ . This point is indicated as point  $P$  in the following, and well represents the spectral characteristics of the whole shear layer flow. Figure 8(b) presents power spectral densities of the wall-pressure measurements for microphone  $m1$ , located under the cusp, microphone  $m5$ , located in the shear layer impingement region, and microphone  $m6$ , located a small distance downstream of microphone  $m5$ , as shown in Figure 1. These microphones well represent the general behavior of the others and will be used as references throughout the paper. The velocity spectrum shows several distinct peaks at the fundamental wind tunnel resonance frequency  $f_{wt} = 150$  Hz and at its higher harmonics. At a frequency of about 82 Hz the weak signature of one of the two modes developing from the bifurcative behavior shown in Figure 7 is also visible.

The wall-pressure spectra of microphones  $m5$  and  $m1$ , in Figure 8(b), are clearly dominated by a peak at the wind tunnel resonance frequency, which represents most of the energy in the signals. For microphone  $m5$  the intensity of the peak is at least one order of magnitude larger, ( $\phi_{p_5}(150) = 2.3 \text{ Pa}^2/\text{Hz}$ ), than for microphones  $m1$  and  $m6$ , ( $\phi_{p_1}(150) = 0.084 \text{ Pa}^2/\text{Hz}$  and  $\phi_{p_6}(150) = 0.059 \text{ Pa}^2/\text{Hz}$ ). The first harmonic, at  $f = 2f_{wt}$  is also clearly evident for all the three microphone with the spectrum of microphone  $m5$  having the highest value. Interestingly, the signature of third harmonic, at  $f = 3f_{wt} = 450$  Hz, is not captured by any the wall-pressure sensors.

Pressure-velocity cross-correlation coefficient functions  $\rho_{up_i}(\tau)$  were computed for each microphone and with each spatial location in the shear layer. For each location, the maximum value of the correlation coefficient function was computed. In Figure 9, the spatial distribution of this peak value is shown, for the same three microphones as above. Figure 9(c), related to microphone  $m6$ , indicates poor correlation levels between the velocity and this pressure signal, mainly because this microphone is located outside the cavity in a region where a wall-bounded flow is starting to develop. On the other hand, higher levels of correlation, of the order of 0.6, are found in a large region when

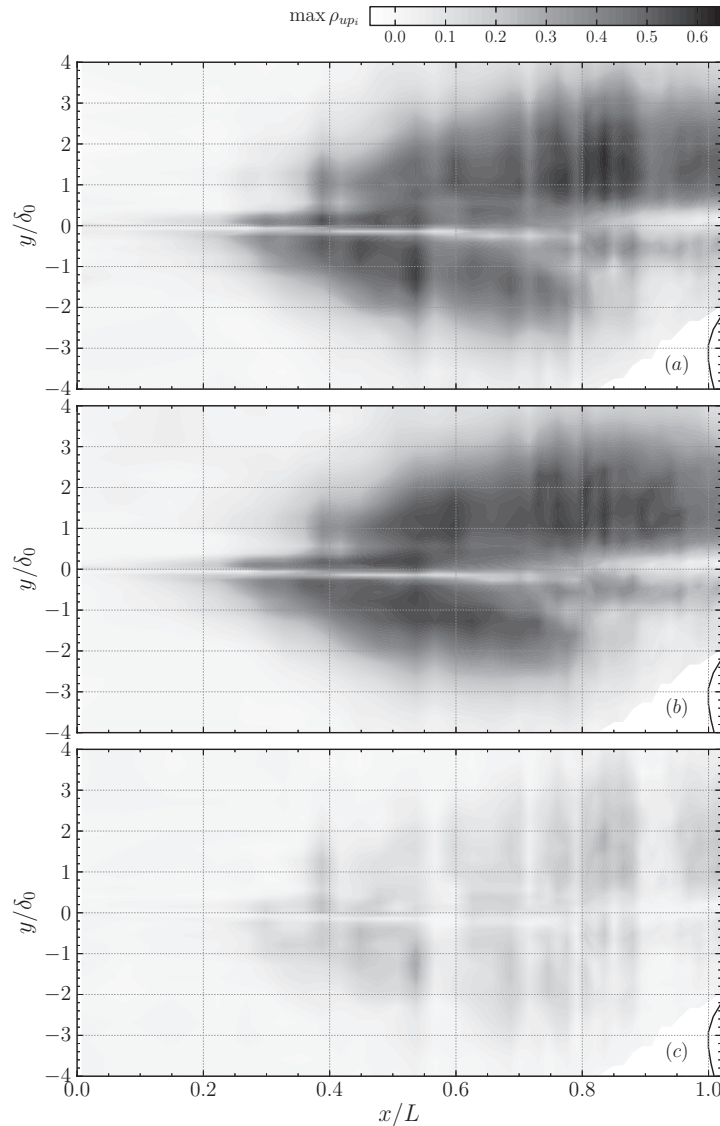


FIG. 9. Contour maps of the maximum cross-correlation coefficient function  $\max \rho_{up_i}(\tau)$  between the velocity and wall-pressure signals, for microphone  $m1$  (a), microphone  $m5$  (b), and microphone  $m6$  (c).

considering both microphones  $m1$  and  $m5$ , Figures 9(a) and 9(b). The distributions for these two microphones show two elongated lobes starting from  $x/L = 0.2$ , located symmetrically around  $y/\delta = 0$ , with the upper lobe extending more downstream. The level of correlation for microphones  $m1$  and  $m5$  grows as the shear layer develops downstream because of the strong amplification of the velocity fluctuations due to the multiple modes of the Kelvin-Helmoltz instability.

In the frequency domain, the correlation between velocity and pressure is expressed by the squared coherence function  $\gamma_{up_i}^2(f)$ , defined as

$$\gamma_{up_i}^2(f) = \frac{|\Phi_{up_i}(f)|^2}{\Phi_u(f)\Phi_{p_i}(f)}, \quad (22)$$

where  $\Phi_{p_i}$  and  $\Phi_u$  are the power spectral density of the  $i$ th microphone pressure signal and of the velocity signal, respectively, and  $\Phi_{up_i}$  is the cross-spectral density between velocity and wall-pressure signals. In Figure 10, squared coherence functions between velocity in the point  $P$  and wall-pressure from the three microphones as before are shown. It can be observed that, for all

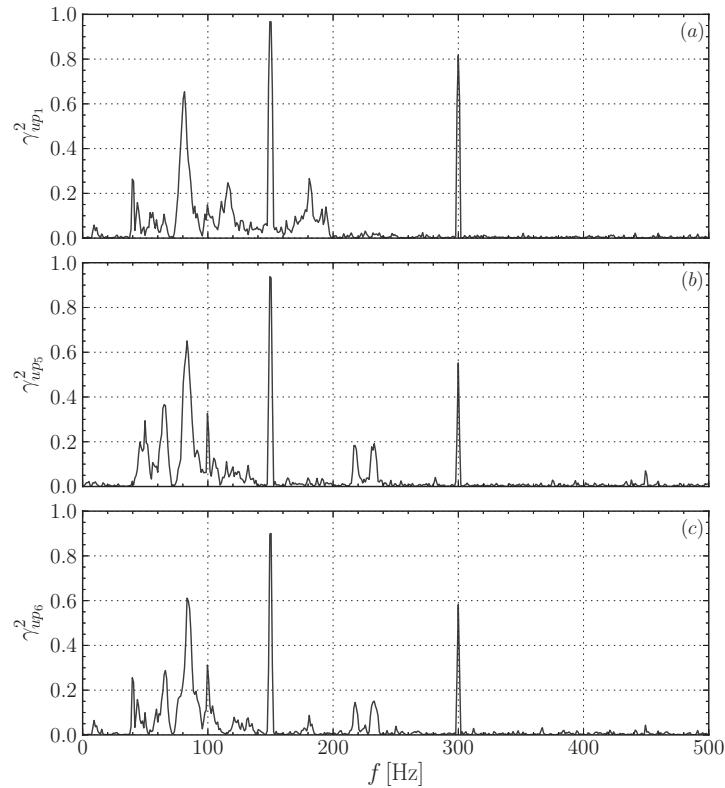


FIG. 10. Squared coherence functions between velocity at point  $P$  and wall-pressure, for three microphones, i.e., microphone  $m1$  (a), microphone  $m5$  (b), microphone  $m6$  (c).

the microphones,  $\gamma_{up_i}^2$  is particularly large at the wind tunnel resonance frequency  $f_{wt}$  and its first harmonic. In the range of frequencies between 0 and 100 Hz, several other peaks can be observed. In particular, the squared coherence presents two peaks at  $f = 63$  and  $82$  Hz, which are due to the bifurcative behavior at the first sub-harmonic of the wind tunnel resonance mode, as discussed for Figure 7. Furthermore, for microphones  $m6$  and  $m5$  there is also some level of coherence at frequencies around  $3/2 f_{wt}$ .

## B. Single-point multi-time-delay stochastic estimation

A discussion regarding the linear and nonlinear single-time-delay stochastic estimation techniques is now first presented. This serves as an introduction of the multi-time-delay approach, discussed later in this section.

The shape of the JPDF between the wall-pressure and velocity fluctuations  $f(p, u)$  was preliminarily investigated in detail, in order to provide some understanding of the relationship between the two variables. As an example of these analyses, Figure 11(a) shows the iso-lines of the JPDF  $f(p_1, u_p)$  of the wall-pressure fluctuations for microphone  $m1$  and of the velocity fluctuations at point  $P$ . Figures 11(c) and 11(b) present the probability density functions (PDF) of the wall-pressure fluctuations from microphone  $m1$  and velocity fluctuations at point  $P$ , respectively. It can be observed that the joint probability density function in Figure 11(a) is strongly non-Gaussian and shows two peaks in opposite locations, a larger one in  $(0.35, 0.65)$ , the other, much weaker and not visible in the figure, around  $(-0.4, -0.7)$ . This bi-modal behavior is mainly due to the oscillatory characteristics of the velocity signal. This is evident in Figure 11(b) where the PDF of the velocity fluctuation signal is clearly characterized by a larger peak at  $u(t) \approx 0.6$  and a much weaker one at  $u(t) \approx -0.85$ . Interestingly, the PDF of the wall-pressure fluctuation measured by microphone  $m1$ , Figure 11(c), is close to normality, with skewness and flatness equal to 0.05 and 2.92, respectively.

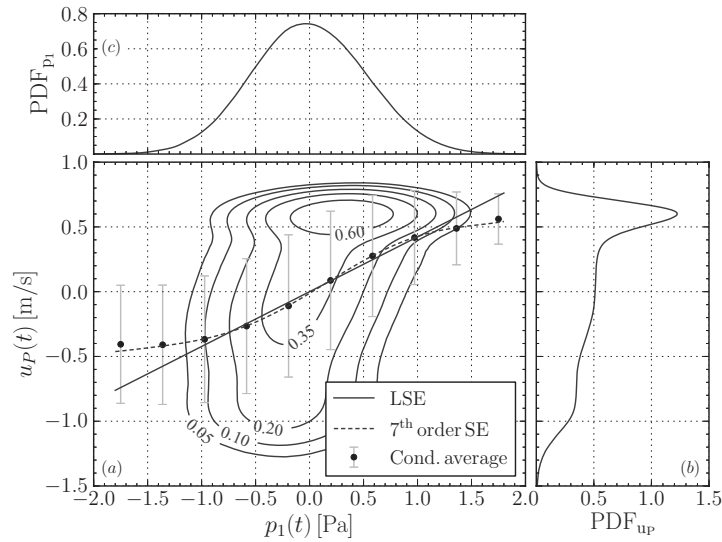


FIG. 11. Joint probability density function  $f(p_1, u_p)$  of the wall-pressure fluctuations from microphone  $m1$  and of the velocity fluctuations at point  $P$ . (a). (c) and (b) show the probability density functions of the wall-pressure fluctuations from microphone  $m1$  and velocity fluctuations at point  $P$ , respectively.

In Figure 11(a), on the same plot of the JPDF, the conditional average of the velocity fluctuations using 10 different wall-pressure events  $E$  using microphone  $m1$  are shown with small black dots. Each point is the conditional average of the velocity fluctuations  $\langle u(t) | E \rangle$ , where event  $E$ , defined as  $p_e - dp < p_1(t) < p_e + dp$ , confines the value of the wall-pressure within a small window of size  $2dp = 0.1$  Pa, centered around  $p_e$  and which varies uniformly between  $-1.75$  and  $1.75$  Pa. For each value of  $p_e$  shown in the figure, the grey error bars represent the standard deviation of the distribution  $f(u | E)$ , i.e., the probability density function of the velocity fluctuations given event  $E$ . This quantity is representative of the scatter of the velocity fluctuations around the conditional average given event  $E$ .

In the same plot, estimates of the velocity obtained using the classical single-time-delay stochastic estimation technique are shown for the linearly truncated expansion of the conditional average (LSE) and for a high order expansion, a seventh order case.

The figure indicates that in the range  $-1$  Pa  $< p_1(t) < 1$  Pa, the linear and high-order approaches provide similar estimates of the conditional average of the velocity fluctuations. However, the nonlinear behavior of the conditional average, clearly evident for  $|p(t)| > 1.3$ , is well captured only by the higher order expansion, which well matches the conditional average value over all the range of wall-pressure events. The better approximation of the conditional average by the high order expansion is clearly due to the non-Gaussianity of the JPDF, as also suggested by Naguib *et al.*<sup>27</sup> and Brereton.<sup>8</sup> In fact, if the JPDF was Gaussian the nonlinear terms of the Taylor expansion of the conditional average would be identically zero. Despite the better approximation of the conditional average by the high order expansion, a small difference in accuracy between the two estimates must be expected, since the probability that  $|p(t)| > 1$  Pa is slight.

It is important to observe that, in the present case, the great length of the error bars in Figure 11 indicates that the conditional average and its approximations via the stochastic approach are not able to accurately describe the velocity fluctuations. This is because the probability density function  $f(u | E)$  shows a large variability of the velocity fluctuations around the conditional average. This variability can be clearly expressed by introducing the normalized mean-square estimation error. This parameter can be obtained by defining  $e(t) = u(t) - \hat{u}(t)$  as the local estimation error, i.e., the difference between the measured velocity value and the estimated velocity value at time  $t$ . By squaring and averaging this equation, and dividing by the variance of the velocity fluctuations

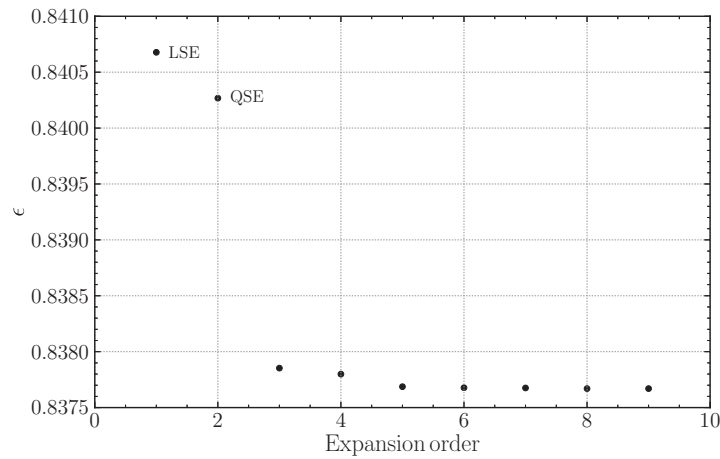


FIG. 12. Normalized mean-square estimation error  $\varepsilon$  of the velocity fluctuations at point  $P$ , for the single-time-delay stochastic estimation as a function of the Taylor expansion order. Microphone  $m1$ .

one obtains

$$\varepsilon = \frac{\overline{e^2}}{\overline{u^2}} = 1 - \frac{\overline{\hat{u}^2}}{\overline{u^2}}, \quad (23)$$

where the second equality holds because of the *orthogonality principle*, in the case where the estimate is obtained by a least-square procedure, Ljung.<sup>24</sup> The parameter  $\varepsilon$  is, therefore, a significant index which describes the fraction of the original variance in  $u(t)$  which has not been recovered by the estimate  $\hat{u}(t)$ . Furthermore,  $\varepsilon$  is bound in  $[0, 1]$ .

In Figure 12, the normalized mean-square estimation error  $\varepsilon$  is reported for stochastic estimates of increasing orders for the velocity fluctuations at point  $P$ , using microphone  $m1$ . It can be clearly observed that there is a sharp decrease in  $\varepsilon$  after order two, then it reaches a plateau after an expansion order equal to 5. This weak drop is due to the change of the sign of the second derivative of the conditional average with respect to the event, which can only be captured by a polynomial in  $p(t)$  of an order larger than 2. It must be noted, however, that there is only a marginal change in the value of  $\varepsilon$  by going from a linear expansion to a fifth order expansion. This clearly indicates that more than 80% of the variance of the velocity fluctuations still cannot be captured by the single time approach, no matter what the expansion order is.

For a multi-time-delay approach, in which  $n$  past samples are considered, one should study the JPDP of the variables  $u(t), p(t), p(t - \Delta t), \dots, p(t - n\Delta t)$ . However, this approach is complicated by the high dimensionality of the problem, which renders this analysis intractable. Nevertheless, the meaning of the  $\varepsilon$  parameter is preserved. In this regard, its value is clearly affected by the number  $n$  of past samples taken for the estimate. In Figure 13, the dependence of  $\varepsilon$  on  $n$  is shown for the single-point estimate of the velocity at point  $P$ , using microphones  $m1, m5$ , and  $m6$ . In this plot, the *single-time-delay* linear stochastic estimation case, which corresponds to  $n = 0$ , is set for graphical convenience at  $n = 0.5$  on the semi-logarithmic plot. The figure clearly indicates that if  $n$  increases the normalized mean-square estimation error decreases remarkably, well below the value reached for the high order single-time-delay stochastic estimation approach in Figure 12. This clearly proves that the multi-time-delay approach is more accurate than classical estimation techniques. The decrease is monotone, starting from a drop-off value  $\tilde{n}$  up to larger values of  $n$ , where an asymptotic value of  $\varepsilon$  is reached for  $n > n^*$ . A different behavior occurs for each microphone. For microphone  $m1$ , and equally for microphones  $m2, m3$ , and  $m4$ , not shown in the figure, the error decreases abruptly after  $n = 20$ , reaching asymptotically a value of  $\varepsilon$  equal to about 0.24. On the other hand, using microphone  $m6$  produces a larger estimation error. This was expected, given the lower correlation of the pressure fluctuations from microphone  $m6$  with the shear layer velocity fluctuations, as reported in Figure 9. Nevertheless, the asymptotic value is practically the same. Microphone  $m5$  shows an

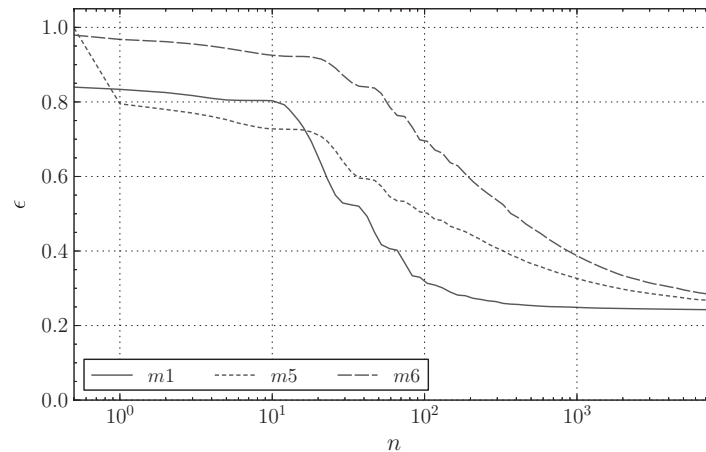


FIG. 13. Normalized mean-square estimation error  $\varepsilon$  of the velocity fluctuations at point  $P$  with respect to the model order, for different microphones.

intermediate behavior and produced lower errors than  $m1$  for  $1 \leq n < 20$ , but larger errors for larger value of  $n$ .

The meaning of the drop-off value  $\tilde{n}$ , of the order of 20 for all the three microphones, is that statistically relevant information which can be used to increase the accuracy of the estimate, only appears after a characteristic time lag  $\tilde{n}\Delta t$ . This can be linked to a time lag for which the cross-correlation function between the velocity and the wall-pressure fluctuations starts to become large. For  $n > \tilde{n}$ , the error decreases strongly at particular values of  $n$  because for the corresponding time lags the cross-correlation function is higher, meaning that important information is contained in the pressure time history for these time delays. On the other hand, the asymptotic behavior which is reached for large values of  $n$ , i.e.,  $n^*$ , may be intuitively explained with the fact that the wall-pressure samples at these large lags in the past are statistically uncorrelated with the velocity fluctuation at time  $t$  and thus they cannot enhance the accuracy of the estimate. Such a threshold time lag can be roughly identified as the time lag for which the cross-correlation function is sufficiently close to zero and, therefore, it may be related to characteristic time scales of the physical mechanisms involved.

It appears clear that a further advantage of the multi-time-delay technique is that it can cope with situations where there is a time lag between the velocity and wall-pressure signals, a problem recognized by Murray and Ukeiley<sup>26</sup> among others, for the classical stochastic estimation approach. In these cases, in fact, the cross-correlation function between these two variables shows a peak for  $\tau \neq 0$ . Therefore, the value of  $n$  can be set as large as is necessary in order to use all the previous samples included in this time lag.

It should be noted that, in the present work, the relatively high value of  $n$  required to achieve a satisfactory accuracy is mainly due to the short sampling interval which was used to acquire the velocity and wall-pressure signals. In a real-time control application this sampling interval must clearly be optimized. It should be sufficiently small to adequately resolve the relevant time scales of the dominant flow mechanisms but as large as possible to reduce the number of past samples used.

The estimation accuracy of the multi-time-delay approach across the whole investigated flow field is presented in Figure 14, which shows the contour map of the distribution of  $\varepsilon(\mathbf{x})$ , for  $n = 1000$ , using microphone  $m1$ . This model order was chosen as it was sufficient to guarantee convergence of  $\varepsilon$  all over the shear layer. The distribution is characterized by two lobes across the shear layer where the estimate is particularly accurate. This distribution closely resembles that of  $\max \rho_{up_1}$ , reported in Figure 9(a), and it replicates many of its features, such as the shape of the two lobes and the thin region where  $\varepsilon$  is high, in  $y/\delta = 0$ . This indicates, as expected, that for a multi-time-delay estimate the mean-square estimation error is smaller if the cross-correlation coefficient function is “large.” A more formal justification of this concept can be obtained by deriving the analytic expression for the

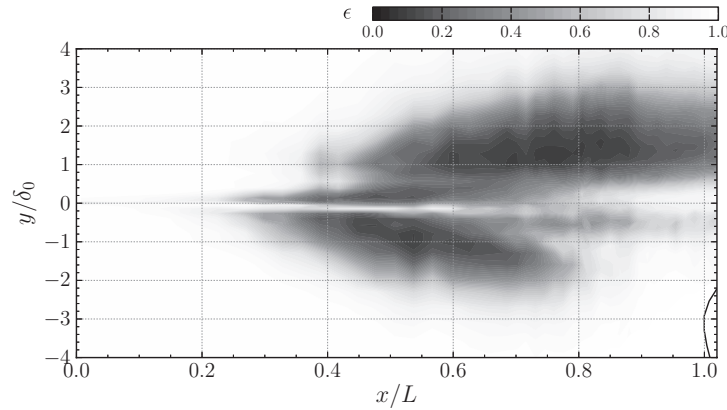


FIG. 14. Contour map of the normalized mean-square estimation error  $\varepsilon$  across the whole shear layer.

normalized mean-square estimation error which reads as<sup>24</sup>

$$\varepsilon = 1 - \frac{1}{u^2} \mathbf{f}^T \mathbf{R}^{-1} \mathbf{f}, \quad (24)$$

where the column vector  $\mathbf{f}$  and the matrix  $\mathbf{R}$  are defined in Eqs. (15) and (14), respectively. In particular, the column vector  $\mathbf{f}$  is made up of the values of the cross-correlation function  $r_{pu}$ , while  $\mathbf{R}$  contains values of the auto-correlation function of the wall-pressure signal. The quadratic form  $\mathbf{f}^T \mathbf{R}^{-1} \mathbf{f}$  is strictly positive, since  $\mathbf{R}$  is a positive definite matrix; furthermore, it depends on  $n$ . This term defines a “size” of the cross-correlation function, which indicates how much information regarding the flow velocity is contained in the wall-pressure time history. For example, if  $\mathbf{R}$  is the identity matrix, that is the case where  $p(t)$  is a unit variance Gaussian noise, the value of the quadratic form reads as

$$\mathbf{f}^T \mathbf{R}^{-1} \mathbf{f} = \mathbf{f}^T \mathbf{f} = \sum_{i=0}^n r_{pu}(i)^2, \quad (25)$$

which is clearly larger if  $r_{pu}$  is large in modulus for as many lags as possible. This expression also justifies the values of  $\tilde{n}$  and  $n^*$ : the error starts to decrease for a value of  $n$  where the summation of Eq. (25) starts to become large, i.e., when the cross-correlation starts to increase. On the other hand, the summation reaches an asymptotic value because, for large  $i$ ,  $r_{pu}(i)$  is close to zero, and no contribution is added by increasing  $i$ . For the general case of  $\mathbf{R}$ , these concepts are still valid even if obtaining the exact expression for  $\mathbf{f}^T \mathbf{R}^{-1} \mathbf{f}$  in terms of  $r_{pu}$  and  $r_{pp}$  is more complicated.

From a theoretical point of view, it can be observed that the fraction of unrecovered variance in the velocity signal, i.e., the remaining 24% of the energy for the case in Figure 13, has two sources. The first is made up of uncorrelated components in the velocity time history. These components cannot be recovered by any kind of technique, since their signature is not present in the wall-pressure time history. The second source of error may be due to a nonlinear relationship in the dynamics between velocity and wall-pressure, which cannot be captured by the proposed approach, which only provides the best linear estimate. In the present analysis, only the linear multi-time-delay stochastic estimation approach was considered, but Eq. (6) can be naturally extended to include high-order nonlinear terms, which will certainly capture nonlinear processes in the flow. However, the extension to high-order terms is more problematic from a numerical point of view, since the problem of finding all the unknown coefficients of the nonlinear expansion suffers from the problem of the “curse of dimensionality” (see Bishop<sup>6</sup>). In fact, in a linear multi-time-delay approach the number of unknown coefficients grows linearly with  $n$ , whereas for an expansion of order two the number of coefficients grows as  $n^2$ , which renders the problem intractable when  $n$  becomes large.

To further highlight the capabilities of the multi-time-delay technique, an example of the reconstruction of the temporal evolution of the velocity is shown in Figure 15. In this figure, a short part of the measured velocity time history at point  $P$  is compared with those estimated

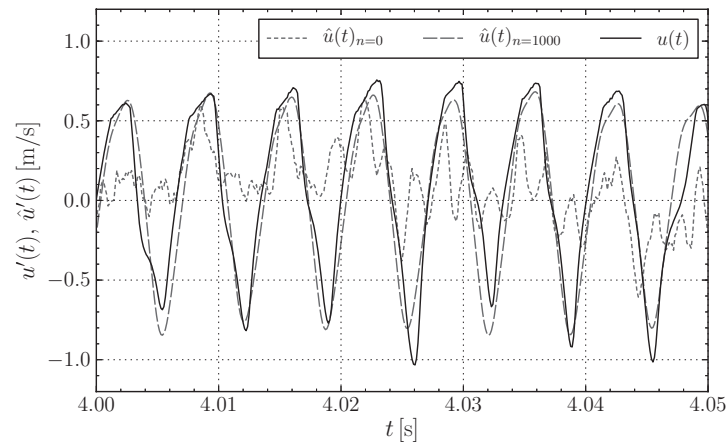


FIG. 15. Detail of the measured and estimated velocity time histories at point  $P$ . The estimates are obtained using microphone  $m1$  and with different model orders, namely,  $n = 0$  (LSE), and  $n = 1000$  (MTD-LSE).

using the classical single-time-delay LSE approach,  $n = 0$ , and the multi-time-delay approach, for  $n = 1000$ . In both cases, microphone  $m1$  was used for the estimate. The accuracy of the estimate for the multi-time-delay approach is markedly higher. The estimated time history closely follows the measured signal, matching both the phase and the amplitude of the dominant oscillation of the shear layer. Furthermore, the frequency content of the estimated time history looks much more similar to that of the measured time history. By contrast, the classical single-time-delay linear stochastic estimation does not faithfully represent the measured velocity signal, missing both the amplitude and the phase of the main oscillation. The improvement of the multi-time-delay approach is even clearer when observing the power spectral densities of the estimation error  $e(t)$ , i.e., the difference between the measured and estimated velocity signals of Figure 15. The spectra are reported in Figure 16, for the STD approach, where  $n = 0$ , and for the MTD approach, where  $n = 1000$ , using in both cases microphone  $m1$  for the estimate.

For the MTD approach the spectral density of the estimation error for the frequencies corresponding to the wind tunnel resonance mode and its first harmonic is at least one order of magnitude lower than that of the single-time-delay approach. The latter fails to recover the main energy contribution in the signal and also produces large errors for a wider range of frequencies. Interestingly, for the multi-time-delay approach in particular, much of the error is concentrated in the side-bands

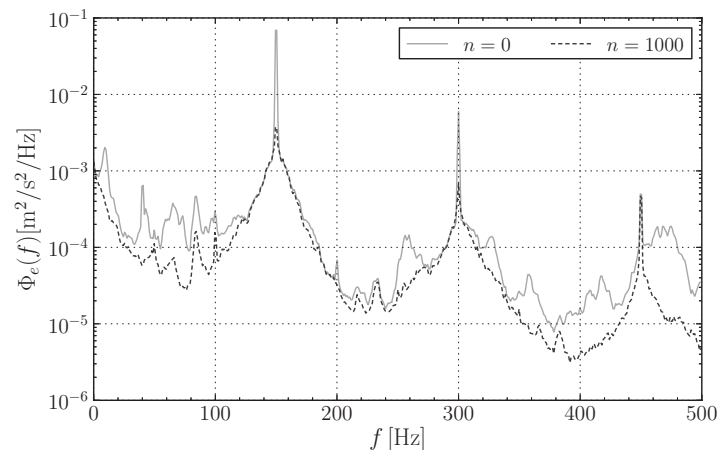


FIG. 16. Power spectral density of the estimation error for the single-time-delay LSE approach,  $n = 0$ , and the multi-time-delay approach, for  $n = 1000$ .

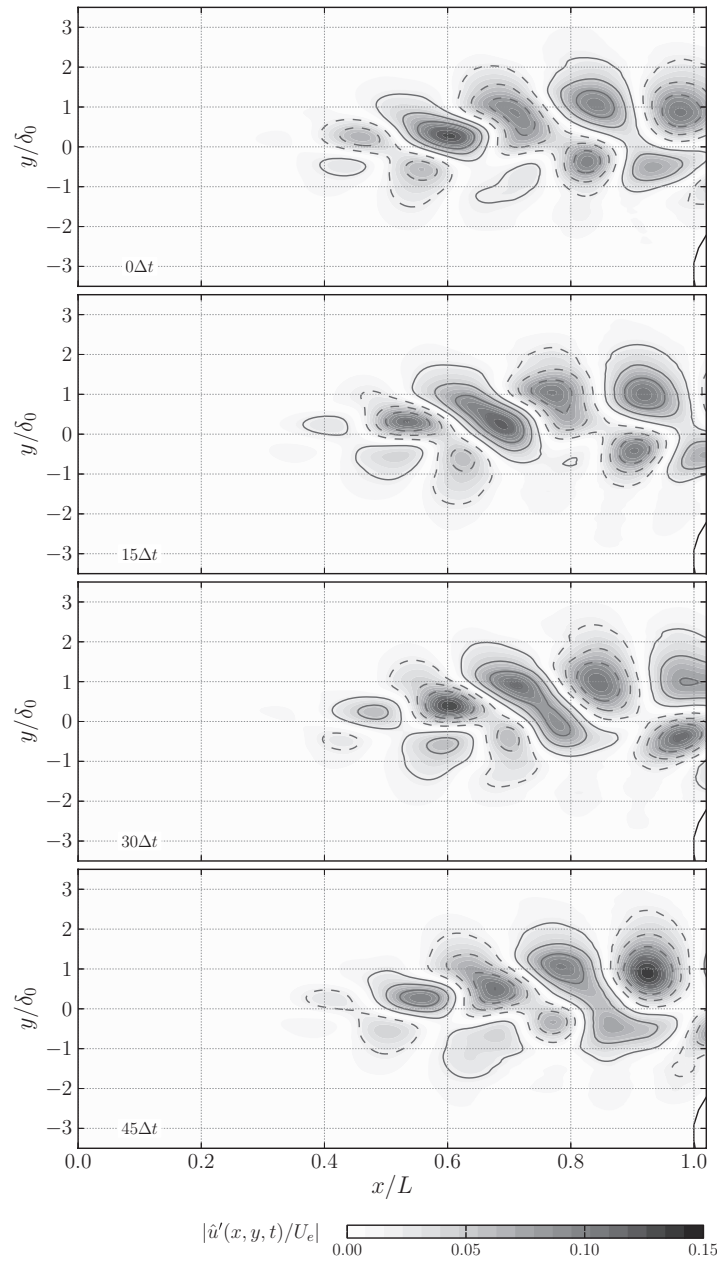


FIG. 17. The contour maps show the reconstructed spatial distribution of the fluctuating velocity component in the shear layer in four selected time instants. The time delay between successive snapshots of the sequence is  $45\Delta t$ , where  $\Delta t = 1/8000$  s is the sampling interval. The grey color shading represents the modulus of the velocity fluctuation. Eight iso-lines have been drawn for values of  $\hat{u}'/U_e$  equal to  $\pm 0.11$ ,  $\pm 0.08$ ,  $\pm 0.05$ ,  $\pm 0.02$ ; dashed contours indicate a negative value.

of the resonance modes. This is connected to the low value of the squared coherence function  $\gamma_{up}^2$  for these frequencies, as evidenced in Figure 10. A further error contribution is also due to lower frequencies, mainly because the microphones significantly attenuate this low range.

Figure 17 shows the time-resolved reconstruction of the spatial distribution of the non-dimensional velocity fluctuation in the shear layer, using the MTD approach with  $n = 1000$ , with microphone  $m1$ . The temporal resolution between successive snapshots is  $45\Delta t$ , i.e., one snapshot out of every 45 reconstructed snapshots is shown. The estimated flow fields were obtained by first computing the  $b_k$  coefficients for every point in the shear layer where a velocity time history was

acquired. Then, the time resolved estimate of the velocity in each point was obtained by using a single wall-pressure time history.

It is clearly visible that the flow field shows a distinct spatial organization characterized by a periodic alternation of regions of positive and negative velocity fluctuation. This feature is a characteristic for a cavity flow in the shear-layer mode, Rowley *et al.*,<sup>32</sup> where the flow is subject to global instability in the form of convective Kelvin-Helmoltz waves excited by feedback from pressure waves generated near the cavity trailing edge. The vertical dimension of the region interested by the phenomenon is comparable to the size of the shear layer estimated from Figure 5.

The convection properties of the coherent structures in the shear layer are also well resolved by the MTD approach. In fact, the coherent structures convection speed ratio  $\kappa = U_c/U_e$  was estimated by performing cross-correlation analyses between estimated velocity time histories in adjacent points at  $y/\delta = \text{constant}$ , for all the point in the shear layer. Examination of the time lag, with respect to the separation  $\Delta x$  between the points, led to a map of  $\kappa$  as a function of the spatial location. The value of  $\kappa$  was almost constant in all the shear layer for  $x/L < 0.7$  and equal to about 0.5, decreasing to about 0.4 only after  $x/L = 0.7$ . These values are in agreement with the previous findings of several authors which investigated flows past rectangular cavities, e.g., Chatellier *et al.*<sup>11</sup>

Results in Figure 17 clearly indicate that the multi-time-delay approach is capable of faithfully reconstructing the flow field structure. This allows a reliable interpretation of the dominant phenomena and of their time evolution. In contrast, if the single-time-delay classical approach had been used for this purpose, the resulting flow field would have lacked much of the physical information obtained with the proposed technique.

### C. Spectral properties of the multi-time-delay estimate

In the frequency domain, the velocity time history estimated with a multi-time-delay approach has important properties, which are highlighted in this section.

For the single-point multi-time-delay estimate of one of the velocity components at a given point  $\mathbf{x}_0$ , we can write that

$$\hat{u}(i) = \sum_{k=0}^n b_k p(i - k), \quad (26)$$

i.e., the estimate of the velocity signal is the convolution of the wall-pressure signal with the vector of coefficients  $b_k$ . By taking the  $z$ -transform of this expression, Hayes,<sup>19</sup> the convolution becomes a multiplication

$$\hat{U}(z) = H(z)P(z), \quad (27)$$

where  $z$  is a complex variable,  $\hat{U}(z)$  and  $P(z)$  are the  $z$ -transforms of the estimated velocity and wall-pressure signals, respectively, while  $H(z)$  is called the *transfer function*, which reads as

$$H(z) = b_0 + b_1 z^{-1} + b_2 z^{-2} + \dots + b_n z^{-n}, \quad (28)$$

i.e., it is a polynomial of order  $n$  in  $z^{-1}$ . The frequency response is obtained by evaluating the transfer function on the unit circle in the complex plane, i.e., for  $z = e^{i2\pi f}$ , obtaining

$$H(e^{i2\pi f}) = |H(e^{i2\pi f})| e^{i\Theta(2\pi f)}, \quad (29)$$

where the real valued *amplitude response*  $|H(e^{i2\pi f})|$  and the *phase response*  $\Theta(2\pi f)$  have been conveniently separated. The amplitude response is important because it relates the spectra of the wall-pressure signal to that of the estimated velocity signal. In fact, it can be shown that these spectra are related by

$$\Phi_{\hat{u}}(f) = |H(e^{i2\pi f})|^2 \Phi_p(f), \quad (30)$$

meaning that each frequency component in the wall-pressure signal is amplified or attenuated in the estimate as dictated by the amplitude response. On the other hand, the phase response  $\Theta(2\pi f)$  provides information regarding the phase difference between the wall-pressure and the estimated

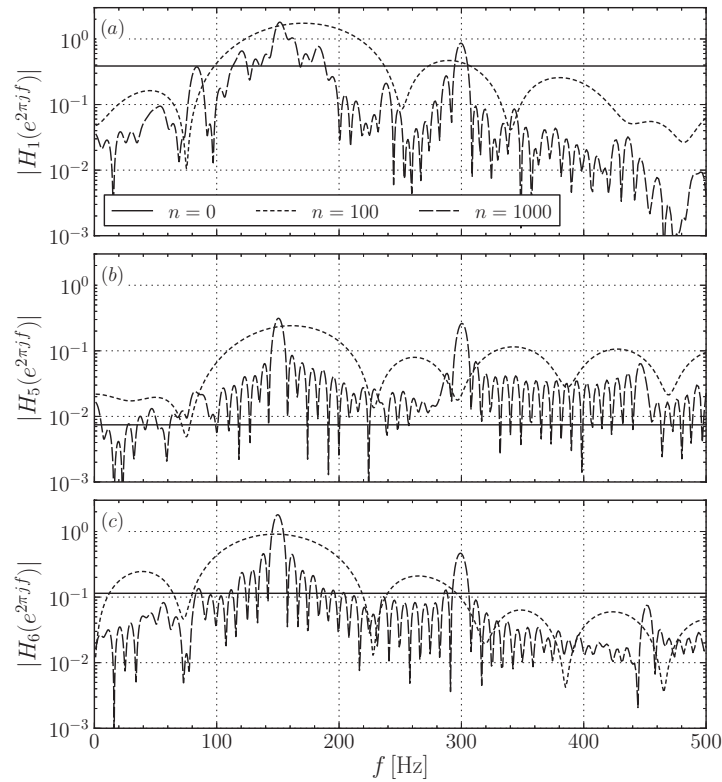


FIG. 18. Amplitude response plots related to estimates of the velocity at point  $P$  using different microphones:  $m1$  – (a),  $m5$  – (b), and  $m6$  – (c). The curves were obtained using different model orders. Note that  $n = 0$  corresponds to the classical single-time-delay linear stochastic estimation approach.

velocity signal at each frequency component. This gives insight regarding the time lags for the important physical mechanisms in the flow.

In Figure 18, the amplitude response  $|H_i(e^{i2\pi f})|$  is shown for different model orders  $n$ . These are related to the estimate of the velocity at point  $P$ , with the same three microphones used previously. It can be seen that the amplitude response is a constant for the single-time-delay linear stochastic estimation approach,  $n = 0$ . This means that all the frequency components in the wall-pressure signal, both noise and “signal” parts are equally scaled, by a factor which is equal to  $b_0^2 = (r_{pu}(0)/r_{pp}(0))^2$ . This property has several drawbacks. In fact, the single-time-delay linear stochastic estimation approach is incapable of reconstructing a velocity field whose spectral characteristics are strongly different from those of the wall-pressure signal. Furthermore, all the noise and incoherent contributions are directly transferred to the estimated velocity field, which has practical consequences in a flow control system, where accurate estimates of the flow state must be available to guarantee satisfactory effectiveness of the control, Cattafesta *et al.*<sup>10</sup>

By contrast, for the multi-time-delay approach, if  $n$  increases, the transfer function gains the capability to selectively attenuate or amplify each frequency component independently. This increased flexibility means that the drawbacks of the single-time-delay linear stochastic estimation approach can be relaxed.

The transfer function coefficients  $b_k$  are not chosen arbitrarily by specifying bandpass properties; they are obtained from a least-square criterion. In this case, it can be demonstrated, Hayes,<sup>19</sup> that for  $n \rightarrow \infty$ , the squared amplitude response of the transfer function of Eq. (28) tends to

$$|H(e^{i2\pi f})|^2 = \gamma_{up}^2(f) \frac{\Phi_u(f)}{\Phi_p(f)}, \quad (31)$$

where  $\Phi_u(f)$  and  $\Phi_p(f)$  are the power spectral densities of the measured velocity and wall-pressure signals, and  $\gamma_{up}^2(f)$  is the squared coherence function, defined in Eq. (22). Equation (31) states that by using the multi-time-delay approach, each frequency component in the pressure signal is first scaled by the factor  $\Phi_u(f)/\Phi_p(f)$ , to recover the energy of the measured velocity signal, but it is then attenuated according to the value of the coherence between the signals, since  $0 \leq \gamma_{up}^2(f) \leq 1$ .

By substituting (31) in Eq. (30), it can be obtained that  $\Phi_{\hat{u}}(f) = \gamma_{up}^2(f)\Phi_u(f)$ , which means that the velocity field estimated using a multi-time delay approach only contains those physical mechanisms which make the velocity and wall-pressure signals strictly correlated. The incoherent contributions are, therefore, eliminated from the estimate. This may be a robust tool for gaining considerable insight in the dynamics of a flow, since the relevant coherent mechanisms responsible for the large pressure fluctuations at the wall can be identified.

It can be also shown, that for  $n \rightarrow \infty$ , the phase response  $\Theta(f)$  of the transfer function of Eq. (29) becomes

$$\Theta(f) = \tan^{-1} \left\{ \frac{\text{Re}\{\Phi_{up}(f)\}}{\text{Im}\{\Phi_{up}(f)\}} \right\}, \quad (32)$$

where  $\text{Re}\{\cdot\}$  and  $\text{Im}\{\cdot\}$  denote the real and imaginary parts of the cross-spectral density  $\Phi_{up}(f)$ . This equation states that, as  $n$  increases, the phase response of the transfer function  $H(e^{i2\pi f})$  of Eq. (28) tends to the phase spectrum of the velocity-pressure joint time histories. The phase spectrum fully contains the phase information regarding the velocity-pressure time histories at each frequency, which can be thus effectively taken into account. This property has fundamental implications for estimates in strongly convective flows, where there is a physical separation between the sensor and the location where the velocity has to be estimated.

The above relations hold exactly for  $n \rightarrow \infty$ . For a finite value of  $n$ , the amplitude and phase responses are just approximations of their respective limit values. However, if  $n$  is sufficiently high, i.e., of the order of  $n^*$ , the approximation becomes more accurate and the properties discussed are effective. Finally, it should be noted that the proposed approach is well known in filtering theory as a finite impulse response Wiener filter.

A brief comparison of the MTD-LSE technique with the SLSE technique detailed by Tinney *et al.*<sup>35</sup> is now discussed. The two techniques have similar features since the transfer function obtained from the MTD approach acts in a similar way to the spectral estimation coefficients of the SLSE approach. In that case, one obtains a spectrum of the reconstructed signal which is exactly the same of that of the original signal at those frequencies where the coherence is greater than an arbitrarily chosen threshold. At other frequencies the spectrum is set to zero, so that only the coherent contributions are retained. In this regard, the multi-time-delay approach shows a fundamental difference. In fact, the MTD approach does not rely on any user chosen threshold but *all* the information available in the wall-pressure signal is optimally used to obtain a minimum square error estimate, in which the coherent components are retained proportionally to the value of the squared coherence function. The multi-time-delay approach may be suited for flow state estimation in a real-time flow control application. In fact, in a flow control system the computational time related with the control algorithm must be smaller than the time scale of the physical mechanisms involved. In the multi-time-delay approach, flow field estimates can be quickly obtained by convolution of the input signals from the sensors with the coefficients  $b_k$  obtained off-line, which is a computationally fast and efficient problem on modern real-time control hardware. From this point of view, using the SLSE approach to obtain flow field estimates requires to perform Fourier transforms of the input signals in the frequency domain, which is a more demanding task.

#### D. Multi-point multi-time-delay stochastic estimation

Investigations were conducted to explore the effects of the number  $M$  of sensors on the accuracy of the multi-time-delay estimate, for several model orders  $n$ . Different sets and combinations of sensors were considered, but because of the large number of these combinations, results for only a limited subset are reported. Figure 19 shows the effects of the model order  $n$  on the normalized

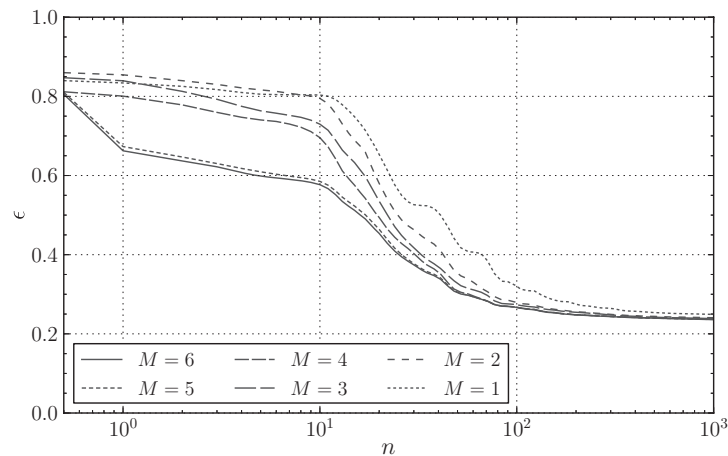


FIG. 19. Normalized mean-square estimation error  $\varepsilon$  for the velocity at point  $P$  with respect to the model order, and for some combinations of  $M$  sensors.

mean-square estimation error  $\varepsilon$ , for the estimate of the velocity at point  $P$ . The curves were obtained using the combinations of sensors reported in Table I. These were the combinations, which for a given  $M$ , yielded the minimum error for  $n = 1000$ , also reported in the same table.

As expected, if the number of sensors used in the estimate is increased, the mean-square estimation error generally decreases. This means that a multi-point approach is more accurate than a single-point technique. This is qualitatively in agreement with previous findings of several authors, e.g., Cole *et al.*<sup>12</sup> among others. These authors considered the multi-point estimate for the classical single-time-delay approach and found it more accurate than the single-point technique. However, the gain obtained by using more than one sensor depends on  $n$  and remarkably decreases if the model order is large, i.e., if  $n > n^*$ . For  $n = 1000$ , the decrease of  $\varepsilon$  brought by using all the six sensors instead of just one is marginal, and of the order of 0.013. The values of  $\varepsilon$  for  $n = 1000$ , reported in Table I, indicate that most of the marginal decrease is obtained for  $M = 2$ , with a smaller effect of adding more than two sensors. There is also a slight gain by going from  $M = 5$  to  $M = 6$ , i.e., by adding microphone  $m_6$  to the estimate. This is due to the low cross-correlation levels between the velocity fluctuations and the wall-pressure fluctuations measured by this microphone.

For  $n < 10$ , the single-point estimate using microphone  $m_1$  appears more accurate than the multi-point estimate with  $M = 2$  (microphones  $m_2, m_4$ ), and  $M = 3$  (microphones  $m_2, m_4, m_3$ ). This is explained by considering that these two combinations of two and three sensors are not the *optimal* combinations for these values of  $n$ . This aspect was investigated in detail for each model order by evaluating the estimation accuracy resulting from all the possible combinations of  $M$  sensors. Results of these analysis, not reported here for the sake of brevity, indicated that in general the optimal combination, for given  $M$ , changes with the model order. Furthermore, it was found that for

TABLE I. Best combinations of  $M$  microphones and corresponding normalized mean-square estimation error for the velocity at point  $P$ , for  $n = 1000$ .

$M$	Combination	$\varepsilon$
1	$m_1$	0.249
2	$m_2, m_4$	0.240
3	$m_2, m_4, m_3$	0.239
4	$m_2, m_4, m_3, m_1$	0.237
5	$m_2, m_4, m_3, m_1, m_5$	0.236
6	$m_2, m_4, m_3, m_1, m_5, m_6$	0.236

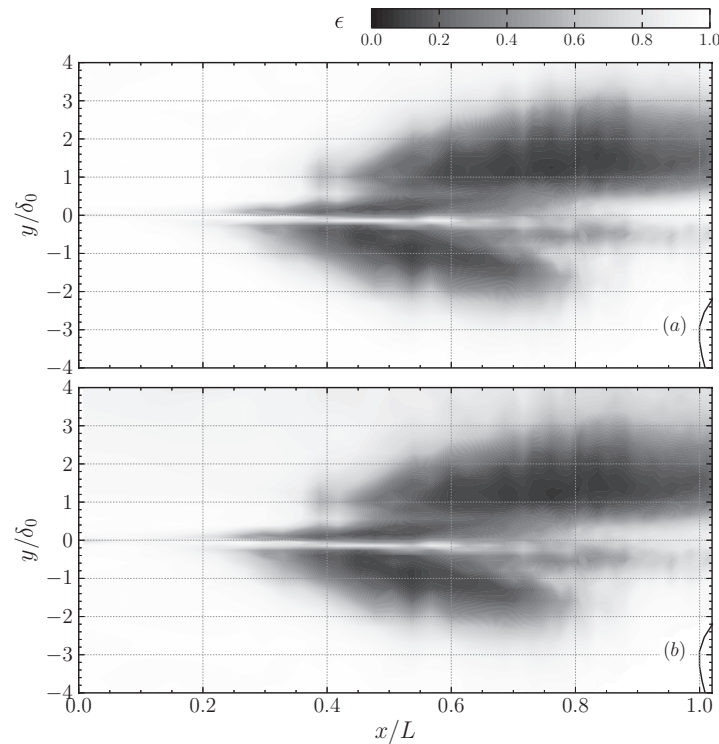


FIG. 20. Contour maps of the normalized mean-square estimation error for the single-point estimate using microphone  $m1$  (a), and for the multi-point estimate using all the six microphones (b). In both cases the model order  $n$  is set to 1000.

all the values of the model order, the estimation accuracy improves monotonically as the number of sensors is increased if the optimal combinations are considered, justifying the apparent contradiction of Figure 19 for  $n < 10$ .

The slight gain introduced by the multi-point estimation for large model orders is a general feature of the whole shear layer flow field. Figure 20 shows contour maps of the distribution of the normalized mean-square estimation error  $\varepsilon$  for the single-point, ( $M = 1$ ), estimate using microphone  $m1$ , Figure 20(a) and for multi-point estimate with  $M = 6$ , Figure 20(b). For both cases the model order is set to 1000, larger than  $n^*$ . It can be observed that in all the flow field the improvement of the multi-point estimate is marginal and both approaches capture then same structure with nearly the same level of accuracy. In fact, in the whole shear layer region the difference in  $\varepsilon$  between the single- and multi-point estimates is not larger than 0.03.

The likely reason for the marginal gain introduced by the multi-point estimate is that, for large model orders  $n$ , most of the required information regarding the flow dynamics is already contained in a single wall-pressure time history. Therefore, if the same information is used two or more times by using two or more sensors measurements, the quality of the estimate cannot improve much.

A further important aspect is related to the computational time required to estimate accurately the flow state, which is an important consideration in a real-time flow control system. If the  $b_{jk}$  coefficients of Eq. (6) have been previously computed off-line, the computational time required for the estimation of the flow velocity at a given location in the flow and at a given time  $t$ , is due, for the multi-time-delay, multi-point technique, to the  $M$  convolution operations of the wall-pressure data with the coefficients vectors. This computational effort is proportional to  $Mn$  and it is thus evident that a compromise between accuracy and computational times must be accepted. In fact, if a larger number of sensors is used, the estimate is more accurate but the associated computational effort is larger and vice versa. In Figure 21, the normalized mean-square estimation error  $\varepsilon$  is reported against the computational time  $Mn$ , for the multi-point case  $M = 6$  and for the single-point case using microphone  $m1$ . It can be seen that in the range  $20 < Mn < 10^3$  the single-point estimate

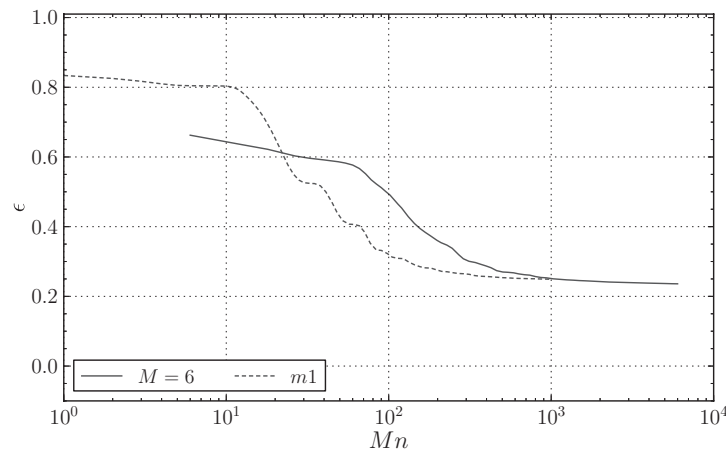


FIG. 21. The normalized mean-square estimation error  $\varepsilon$  is plotted against the computational effort  $Mn$  required for flow state estimation at a single spatial location, for the single- and multi-point multi-time-delay approaches.

produces a more accurate reconstruction of the flow field for a given computational effort. The same consideration applies if a given error limit  $\varepsilon$  is set: in this case, the estimate is less computationally expensive for the single-point case. This suggests that from a control point of view, for a cavity flow one sensor may be sufficient to reproduce with sufficient accuracy and with short computational times the relevant dynamics of the shear layer. In addition a single sensor approach would also limit the complexity and the costs of the setup.

It should be noted that the number of sensors required for accurate flow estimation may depend on the specific flow investigated. In fact, in this case the shear layer flow is predominantly driven by the Kelvin-Helmholtz instability, a large scale organized phenomenon, well captured by the multi-time-delay approach with a single sensor. Bluff bodies wakes and separating flows are also other examples of flow fields where large scale organized structures are present which make the velocity and wall-pressure highly correlated. On the other hand, a wall bounded flow exhibits a much more complex organization, with a wide range of time and length scales. In this case, it is probable that a larger number of sensor would be required to estimate the velocity field in large regions of the flow, despite a multi-time-delay approach.

## V. CONCLUSIONS

In this paper, the multi-time-delay, single- and multi-point linear stochastic estimation technique has been further developed and described in detail. It has been applied as a demonstration to the estimate of the temporal evolution of the velocity fluctuation in a cavity shear layer, based on wall-pressure measurements. The proposed technique may provide a powerful tool in applications such as modeling, prediction, and control of complex flows. In fact, properties highlighted in the paper, such as low estimation error, low number of sensors required, and the low computational effort, are key features in a flow control system, where accurate reconstruction of the spatio-temporal dynamics of the flow and of its driving physical mechanisms is required.

In the paper, it is clearly demonstrated that the multi-time-delay approach outperforms the classical linear and nonlinear single-time-delay stochastic estimation technique in terms of mean-square estimation error, producing a remarkable improvement in accuracy. In addition, this improvement strongly depends on the number  $n$  of past samples of the wall-pressure time history taken into account.

We also show that, in the spectral domain, the multi-time-delay linear stochastic estimation technique produces estimated velocity time histories whose spectral content closely match that of the time histories measured. This feature cannot be achieved by the classical single-time-delay stochastic estimation approach, which produces a power spectrum of the estimated velocity time

history by scaling the wall-pressure power spectrum by a constant. Furthermore, in the MTD-LSE approach the phase lag between the velocity and wall-pressure time histories is taken into account at each frequency, which means that it can cope with situations where the sensor and the estimation location are separated by a physical distance.

With respect to the SLSE technique, the multi-time-delay approach eliminates the need to choose a threshold to select the coherent frequency components to be retained in the estimate. The same effect is achieved, for large  $n$ , by retaining each frequency component proportionally to the level of the squared coherence between the velocity and wall-pressure. As a consequence, the proposed technique makes use of *all* the available spectral information in the wall-pressure time history, resulting in a minimum mean-square estimation error.

The multi-point, multi-time-delay linear stochastic estimation technique was also investigated in detail. It was shown that, if  $n$  is large, the improvement in accuracy brought by using measurements from multiple sensors is marginal with respect to the single-point case. This is explained by the fact that the information needed to capture the important dynamics of the shear layer flow is already contained in a single wall-pressure time history, and can be taken into account by using multiple past values of the wall-pressure time history. Furthermore, the computational effort required to estimate the flow field with the same level of accuracy was lower for the single-point case with respect to the multi-point case.

This technique may offer invaluable insight into the spatio-temporal evolution of coherent structures. In fact, the spatio-temporal evolution of the whole shear layer flow field was faithfully reconstructed by the MTD-LSE technique and the dominant flow mechanism, i.e., the Kelvin-Helmholtz instability of the shear layer, was clearly captured.

An important question for future studies will be to develop a nonlinear multi-time-delay stochastic estimation technique. In fact, a high-order approach is required to fully capture nonlinear processes in the flow, thus providing a more accurate identification and reconstruction of these mechanisms.

## ACKNOWLEDGMENTS

The authors wish to thank the technicians Marco Grivet and Marco Cannata for their precious help during the experiments.

- <sup>1</sup>R. J. Adrian, "On the role of conditional averages in turbulence theory," in *Turbulence in Liquids, Proceedings of the Fourth Biennial Symposium*, Rolla, MO, 22–24 September 1975 (A77-40426 18-34), edited by J. L. Zakin and G. K. Patterson (Science Press, Princeton, N.J., 1977), pp. 323–332.
- <sup>2</sup>R. J. Adrian and P. Moin, "Stochastic estimation of organized turbulent structure: Homogeneous shear flow," *J. Fluid Mech.* **190**, 531–559 (1988).
- <sup>3</sup>AGARD-AR-336, *Wind Tunnel Wall Corrections* (NATO Research and Technology Organisation, 1998).
- <sup>4</sup>J. S. Bendat and A. G. Piersol, *Random Data: Analysis and Measurement Procedures* (Wiley, 1986).
- <sup>5</sup>G. Berkooz, P. Holmes, and J. L. Lumley, "The proper orthogonal decomposition in the analysis of turbulent flows," *Annu. Rev. Fluid Mech.* **25**, 539–575 (1993).
- <sup>6</sup>C. M. Bishop, *Neural Networks for Pattern Recognition* (Clarendon, 1995).
- <sup>7</sup>J. P. Bonnet, D. R. Cole, J. Delville, M. N. Glauser, and L. S. Ukeiley, "Stochastic estimation and proper orthogonal decomposition: Complementary techniques for identifying structure," *Exp. Fluids* **17**, 307–314 (1994).
- <sup>8</sup>G. J. Brereton, "Stochastic estimation as a statistical tool for approximating turbulent conditional averages," *Phys. Fluids A* **4**(9), 2046–2054 (1992).
- <sup>9</sup>L. N. Cattafesta, S. Garg, M. Choudari, and F. Li, "Active control of flow-induced cavity resonance," AIAA Paper No. 97-1804, 1997.
- <sup>10</sup>L. N. Cattafesta, Q. Song, D. Williams, C. Rowley, and F. Alvi, "Active control of flow-induced cavity oscillations," *Prog. Aerosp. Sci.* **44**, 479–502 (2008).
- <sup>11</sup>L. Chatellier, J. Laumonier, and Y. Gervais, "Theoretical and experimental investigations of low mach number turbulent cavity flows," *Exp. Fluids* **36**, 728–740 (2004).
- <sup>12</sup>D. R. Cole, M. N. Glauser, and Y. G. Guezennec, "An application of the stochastic estimation to the jet mixing layer," *Phys. Fluids A* **4**(1), 192–194 (1992).
- <sup>13</sup>R. Donelli, P. Iannelli, S. Chernyshenko, A. Iollo, and L. Zannetti, "Design and analysis of vortex cells," *AIAA J.* **47**(2), 451–467 (2009).
- <sup>14</sup>V. Durgesh and J. W. Naughton, "Multi-time-delay LSE-POD complementary approach applied to unsteady high-Reynolds-number near wake flow," *Exp. Fluids* **49**, 571–583 (2010).
- <sup>15</sup>D. Ewing and J. Citriniti, "Examination of a LSE/POD complementary technique using single and multi-time information in the axisymmetric shear layer," in *Proceedings of the IUTAM Symposium on Simulation and Identification of Organized Structures in Flows*, Kluwer, Lyngby, Denmark, 25–29 May 1997 (Springer, Netherlands, 1997), pp. 375–384.

- <sup>16</sup> A. Garcia-Sagrado and T. Hynes, "Stochastic estimation of flow near the trailing edge of a NACA0012 airfoil," *Exp. Fluids* **51**, 1057–1071 (2011).
- <sup>17</sup> M. Gharib and A. Roshko, "The effect of flow oscillations on cavity drag," *J. Fluid Mech.* **177**, 501–530 (1987).
- <sup>18</sup> Y. G. Guezennec, "Stochastic estimation of coherent structures in turbulent boundary layers," *Phys. Fluids A* **1**, 1054–1060 (1989).
- <sup>19</sup> M. H. Hayes, *Statistical Digital Signal Processing and Modeling* (Wiley, 1996).
- <sup>20</sup> A. Hokpunna and M. Manhart, "A large-eddy simulation of vortex cell flow with incoming turbulent boundary layer," *Int. J. Mech. Syst. Sci. Eng.* **1**, 123–128 (2007).
- <sup>21</sup> L. M. Hudy, A. Naguib, and W. M. Humphreys, "Stochastic estimation of a separated-flow field using wall-pressure-array measurements," *Phys. Fluids* **19**(2), 024103 (2007).
- <sup>22</sup> M. O. Iqbal and F. O. Thomas, "Coherent structure in a turbulent jet via a vector implementation of the proper orthogonal decomposition," *J. Fluid Mech.* **571**, 281–326 (2007).
- <sup>23</sup> D. Lasagna, R. Donelli, F. De Gregorio, and G. Iuso, "Effects of a trapped vortex cell on a thick wing airfoil," *Exp. Fluids* **51**, 1–16 (2011).
- <sup>24</sup> L. Jung, *System Identification: Theory for the User* (Prentice-Hall, 1999).
- <sup>25</sup> N. E. Murray and L. S. Ukeiley, "Estimation of the flowfield from surface pressure measurements in an open cavity," *AIAA J.* **41**(5), 969–972 (2003).
- <sup>26</sup> N. E. Murray and L. S. Ukeiley, "Modified quadratic stochastic estimation of resonating subsonic cavity flow," *J. Turbul.* **8**, N53 (2007).
- <sup>27</sup> A. M. Naguib, C. E. Wark, and O. Juckenhofel, "Stochastic estimation and flow sources associated with surface pressure events in a turbulent boundary layer," *Phys. Fluids* **13**(9), 2611 (2001).
- <sup>28</sup> W. F. J. Olsman, J. F. H. Willems, A. Hirschberg, T. Colonius, and R. R. Trieling, "Flow around a NACA0018 airfoil with a cavity and its dynamical response to acoustic forcing," *Exp. Fluids* **51**, 493–509 (2011).
- <sup>29</sup> C. Picard and J. Delville, "Pressure velocity coupling in a subsonic round jet," *Int. J. Heat Fluid Flow.* **21**(3), 359–364 (2000).
- <sup>30</sup> J. T. Pinier, J. M. Ausseur, and M. N. Glauser, "Proportional closed-loop feedback control of flow separation," *AIAA J.* **45**(1), 181–190 (2007).
- <sup>31</sup> J. E. Rossiter, "Wind-tunnel experiments on the flow over rectangular cavities at subsonic and transonic speeds," Aeronautics Research Council Report No. 3438, 1964.
- <sup>32</sup> C. W. Rowley, T. Colonius, and A. J. Basu, "On self-sustained oscillations in two-dimensional compressible flow over rectangular cavities," *J. Fluid Mech.* **455**, 315–346 (2002).
- <sup>33</sup> C. W. Rowley, V. Juttijudata, and D. R. Williams, "Cavity flow control simulations and experiments," AIAA Paper No. 2005-292, 2005.
- <sup>34</sup> V. Sarohia, "Experimental and analytical investigation of oscillations in flows over cavities," Ph.D. dissertation (California Institute of Technology, 1975).
- <sup>35</sup> C. E. Tinney, F. Coiffet, J. Delville, A. M. Hall, P. Jordan, and M. N. Glauser, "On spectral linear stochastic estimation," *Exp. Fluids* **41**, 763–775 (2006).
- <sup>36</sup> T. C. Tung and R. J. Adrian, "Higher-order estimates of conditional eddies in isotropic turbulence," *Phys. Fluids* **23**(7), 1469 (1980).
- <sup>37</sup> L. Ukeiley and N. Murray, "Velocity and surface pressure measurements in an open cavity," *Exp. Fluids* **38**, 656–671 (2005).
- <sup>38</sup> L. Ukeiley, N. Murray, Q. Song, and L. Cattafesta, "Dynamic surface pressure based estimation for flow control," *IUTAM Symposium on Flow Control and MEMS* (Springer, 2008), pp. 183–189.
- <sup>39</sup> K. Zhang and A. M. Naguib, "Effect of finite cavity width on flow oscillation in a low-mach-number cavity flow," *Exp. Fluids* **51**, 1–21 (2011).